International Journal of Mechanical Sciences 326 (2026) 111894

Contents lists available at ScienceDirect

International Journal of Mechanical Sciences

journal homepage: www.elsevier.com/locate/ijmecsci

Uncovering size effects in crack compliance in nanobeams using MD simulations

Akbar Hassanpour, Hossein Darban *

Institute of Fundamental Technological Research, Polish Academy of Sciences, Pawińskiego 5B, 02-106 Warsaw, Poland

ARTICLE INFO

Keywords:
Molecular dynamics
Nonlocal elasticity theory
Nanobeams
Crack compliance
Size effect
Silicon

ABSTRACT

The effect of a crack on the structural response of a nanobeam is commonly modeled by introducing a discontinuity in the slope at the cracked cross-section, with the magnitude proportional to the bending moment transmitted through the section. The proportionality factor (i.e., the crack compliance) is typically derived from closed-form solutions based on classical linear elastic fracture mechanics, whose validity at micro- and nanoscale dimensions is not well established. This study reveals size effects in the crack compliance of silicon nanobeams by integrating large-scale molecular dynamics (MD) simulations involving >2.3 million atoms with beam formulations derived from a local/nonlocal stress-driven gradient elasticity theory. Size-dependent bending and free transverse vibration responses of intact nanobeams are obtained through MD simulations and used to calibrate the nonlocal parameters of the continuum models. The calibrated models are then employed to study cracked nanobeams. Comparisons between MD predictions and theoretical results reveal pronounced size effects: classical formulas substantially underestimate crack-induced flexibility in nanobeams, while the discrepancy decreases with increasing beam length. We demonstrate that this size-dependent crack compliance is influenced by both the crystallographic orientation and the imposed boundary conditions. An atomic strain analysis reveals that the near-tip strain distribution in short nanobeams deviates from the classical $r^{-1/2}$ singular form; however, for sufficiently long nanobeams (e.g., $L \approx 180$ nm for a fixed–guided nanobeam under bending), discrete atomic effects become negligible, and strain distribution and crack compliance converge toward classical predictions.

1. Introduction

The growing field of miniaturization has placed micro- and nanoscale systems and devices at the forefront of innovation. Micro- and nanostructures, such as miniaturized beams, shells, and plates, have attracted significant attention in recent decades due to their critical role in emerging micro- and nanoscale technologies. These small-scale structures are increasingly employed in the micro- and nanoelectromechanical systems (MEMS and NEMS) for a wide range of applications [1–7]. In MEMS and NEMS, electrical components are integrated with miniaturized mechanical elements to perform critical functions, including switching, actuation, and sensing [8–14]. The performance, sensitivity, and reliability of many MEMS and NEMS devices are directly governed by the mechanical behavior of the structural components.

1.1. Size effect in mechanical response of nanobeams

Experimental observations and atomistic simulations have revealed that when the dimensions of a beam decrease to the micro- or nanoscale, its mechanical response becomes size-dependent [15–23]. The size effect generally appears in two distinct forms. In some cases, a softening behavior is observed, where the effective elastic properties decrease with reducing beam dimensions [24–29]. In contrast, a stiffening size effect may occur, resulting in enhanced elastic properties such as increased bending stiffness, natural frequencies, and Young's modulus compared to a large-scale beam [30–35].

In general, size effects observed in micro- and nanostructures are classified as intrinsic or extrinsic. Intrinsic size effects originate from characteristic material length scales associated with the microstructure, such as grain size and boundaries [36]. As the structural dimensions become comparable to these characteristic lengths, the deformation mechanisms deviate from those assumed in classical continuum mechanics [37].

* Corresponding author.
E-mail address: hdarban@ippt.pan.pl (H. Darban).

https://doi.org/10.1016/j.ijmecsci.2026.111894
Received 16 December 2025; Received in revised form 3 June 2026; Accepted 2 July 2026
Available online 5 July 2026

Extrinsic size effects, in contrast, arise from geometric and surface-related phenomena rather than from the internal microstructure of the material. At the micro- and nanoscale, the surface-to-volume ratio increases significantly, causing surface effects to influence the mechanical response strongly. Surface atoms experience broken bonds, reduced coordination numbers, and altered electronic environments compared with bulk atoms [38–40]. Consequently, surface-related interactions become increasingly important and may introduce a size effect in the mechanical response [41–44]. Previous atomistic studies have shown that surfaces may behave either as elastically stiffer or softer layers, depending on the balance between electron density redistribution and coordination loss effects [45]. For silicon, it is demonstrated that surface effects can reduce the effective stiffness [46].

1.2. Modeling techniques

Classical elasticity theory assumes that the stress at a material point depends only on the strain at that same point. This local constitutive assumption neglects interactions occurring over finite spatial distances and therefore cannot capture size effects. As a consequence, classical continuum models may fail to accurately describe the mechanical behavior of structures whose dimensions approach the micro- or nanoscale.

To address these limitations, several nonclassical continuum theories have been developed, including the nonlocal theory of elasticity [47], strain gradient theory [48], couple stress theory [49–51], surface elasticity theory [52,53], and theory of micropolar elasticity [54].

Among these approaches, the nonlocal elasticity theory originally proposed by Eringen [47] has received considerable attention. Nevertheless, Eringen's nonlocal strain-driven model faces certain challenges when its differential form is employed for numerical implementation. For example, it was shown that the response of an Euler–Bernoulli cantilever beam based on Eringen's theory does not exhibit nonlocal effects [55]. To address this limitation, the stress-driven nonlocal theory of elasticity was introduced by modifying Eringen's constitutive equation [56]. This modification resolves the ill-posedness associated with the original nonlocal strain-driven model. However, the purely nonlocal stress-driven formulation is only capable of capturing stiffening behavior at small scales, since it incorporates a single material length scale parameter. Subsequently, this formulation was extended to include additional length scale parameters, enabling the description of both softening and stiffening size effects. This was achieved by introducing a gradient length scale parameter associated with softening behavior, along with a mixture parameter that controls the relative contributions of local and nonlocal effects in the constitutive relation. The resulting model, referred to as the local/nonlocal stress-driven gradient elasticity (SDGE) model [57], is well-posed, free from inconsistencies, and capable of capturing both softening and stiffening behaviors in small-scale structures. The SDGE model has attracted considerable attention and has been widely applied to investigate the mechanical response of micro- and nanoscale structures, including vibration [58], bending [59,60] and buckling [61,62].

1.3. Current limitations in modeling cracked nanobeams

Small-scale structures are susceptible to defects such as cracks, which can significantly reduce their stiffness and natural frequencies [63]. Structural health monitoring (SHM) is essential for ensuring the safety, reliability, and serviceability of structural components. A key aspect of SHM is crack detection, as cracks introduce local flexibility, reduce structural stiffness and natural frequencies, and alter both static and dynamic behaviors. In problems involving mechanical elements such as beams, cracks are often modeled as massless elastic springs. In this approach, a cracked beam is represented as two sub-beams connected at the crack location through rotational and translational springs. The corresponding spring compliances are typically derived from classical fracture mechanics formulations based on local elasticity theory. However, these formulations do not account for size effects and are inherently size independent. For cracked nanobeams, the surface effect is pronounced because the crack introduces additional free surfaces and undercoordinated atoms near the crack tip. These newly generated surfaces act as additional compliant or stiff zones that change the local flexibility around the crack. As a result, the crack compliance may become size-dependent and deviate from classical size-independent predictions, particularly for short nanobeams, where surface effects dominate the overall mechanical response.

Previous studies have investigated the size dependency of linear elastic fracture mechanics using nonlocal, gradient, or surface elasticity formulations, e.g., [64–66]. In addition, experimental investigations have reported size-dependent fracture toughness at the micro- and nanoscale [67–69], indicating that fracture behavior may deviate from the predictions of classical size-independent continuum mechanics as structural dimensions decrease. Despite these prior efforts, the size-dependence of crack compliance for nanobeam formulations has not been explicitly addressed. Due to this gap, conventional, size-independent classical relations continue to be routinely applied in the analysis of small-scale beams.

For example, the transverse vibration of multi-cracked non-uniform Timoshenko beams has been analyzed using size-independent elastic spring models [70]. Similarly, vibration analyses of cracked Timoshenko nanobeams incorporating flexoelectric effects [71], as well as vibration of cracked bi-directional functionally graded nanobeams, have relied on classical crack compliance formulations [72]. Additional studies have addressed the bending response of cracked functionally graded nanobeams [73], along with the vibration behavior of cracked nanobeams and microbeams under various conditions, including elastic foundations, thermal environments, and magnetic fields [74–77].

In all these works, the crack is typically modeled using an equivalent spring representation. However, as size effects emerge at the micro- and nanoscales, the use of size-independent crack compliance raises a critical question: are classical crack compliance formulations reliable at small scales? More specifically, how significant are size effects on crack compliance in nanostructures?

1.4. Objectives and original contributions

To the best of the authors' knowledge, no previous study has directly quantified or revealed the size effect in nanoscale crack compliance using experiments or atomistic simulations. This study aims to address this scientific gap by exploring the size effect on crack compliance in small-scale beams under static bending and free transverse vibration. For this purpose, intact and cracked silicon nanobeams are considered as a representative case study. Silicon is one of the most widely used materials in MEMS and NEMS technologies [78,79], which exhibits a softening behavior at the nanoscale [25,27,80]. Therefore, studying their mechanical behavior requires a model capable of capturing this response. The SDGE model was selected in the present study because it is well-posed, computationally efficient, and capable of describing both stiffening and softening size-dependent responses. In addition to the SDGE model, large-scale molecular dynamics (MD) simulations involving $>$2.3 million atoms are employed, as they provide reference data for the calibration of the SDGE model and enable the assessment of size dependence in crack compliance. MD simulations offer a detailed atomistic perspective on the response of nanostructures. MD has been widely used to investigate a broad range of problems, including the mechanical behavior of silicon nanobeams and nanoplates [19,81].

The structure of the paper is as follows. Section 2 introduces the problem and outlines the classical evaluation of crack compliance and the SDGE model used to analyze the bending and free transverse vibration of nanobeams. Section 3 describes the MD simulations of intact and cracked silicon nanobeams. Section 4 presents and discusses the results, including calibration of SDGE models based on MD data and an

investigation of size effects on crack compliance. Section 5 discusses the limitations and future outlook, while Section 6 concludes the paper with a summary of the main findings.

2. Problem definition and assumptions

To examine the size effect on crack compliance, Euler-Bernoulli nanobeams with rectangular cross-section containing one edge crack are considered. A fixed–guided nanobeam for bending and a cantilever nanobeam for free transverse vibration are studied, as illustrated in Fig. 1(a) and 1(b), respectively. Each beam has an in-plane thickness of H, an out-of-plane width of W, a length of L, and a cross-sectional area of A. A Cartesian coordinate system $x-y$ is established at the mid-thickness of the beam, with the origin at the left end. The crack has a length of a_1 and is located at the position x_1 along the length of the beam. The local bending compliance of the beam is given by $C = \frac{1}{EI}$, where E is the Young's modulus and I is the second moment of the area, defined as $I = \frac{WH^3}{12}$. The mass per unit length is denoted by I_0, and $I_2 = \frac{I_0 H^2}{12}$.

All nanobeams have a square cross-section with $W = H = L/12$, resulting in a slenderness ratio of $L/H = 12$. This geometry falls within the commonly accepted range for Euler–Bernoulli beam theory, where bending deformations dominate, and shear deformations can be neglected. Consequently, the cracked cross-section can be modeled only by a rotational spring, a simplification that allows us to demonstrate the size effects in crack compliance clearly. Additionally, the Euler–Bernoulli theory is integrated with the SDGE nonclassical continuum model, which incorporates material length scale parameters to capture size-dependent behavior at the micro- and nanoscale. Although direct experimental evidence is currently unavailable, similar nonclassical Euler–Bernoulli formulations have been successfully used to describe experimental results for intact micro- and nanobeams [28,35,82–87].

2.1. Classical evaluation of crack compliance

This section summarizes the classical formulation for the crack compliance developed in [88]. To investigate the mechanics of beams containing edge cracks, the elastic spring model, illustrated in Fig. 1(c) and 1(d), is commonly employed. In this approach, a cracked slender beam can be modeled by considering two beam segments connected through a massless elastic rotational spring located at the cracked section, with compliance C_θ. The impact of the crack on the static and dynamic behavior of the structure is accounted for by introducing discontinuity in the cross-section rotation $(\theta = \theta_2 - \theta_1)$ at the crack location. This discontinuity is proportional to the bending moment (M) transmitted across the cracked section:

$$\theta = C_\theta M_{crack}. \tag{1}$$

The crack compliance is derived by equating the mode I strain energy release rate from fracture mechanics to that associated with the equivalent rotational spring [88]:

$$G = \frac{K_I^2}{E'} = \frac{M^2}{2W}\frac{dC_\theta}{da}, \tag{2}$$

where $E' = E$ for plane stress, and $E' = \frac{E}{1-\nu^2}$ for plane strain, where ν is the Poisson ratio.

Using Eq. (2), the rotational compliance C_θ can be written as [88]:

$$C_\theta = \frac{2W}{E'}\int_0^{a_1}\left(\frac{K_I}{M}\right)^2 da. \tag{3}$$

The stress intensity factor K_I, which can be found in fracture mechanics handbooks, is given as:

$$\begin{aligned} K_I &= \frac{6M}{WH^2}\sqrt{\pi a_1}\,F_M(\xi) \qquad \text{for} \quad 0 \le \xi \le 0.6 \\ K_I &= \frac{3.99M}{WH^{3/2}\sqrt{(1-\xi)^3}} \qquad \text{for} \quad 0.6 < \xi < 1 \end{aligned}. \tag{4}$$

Here, $\xi = \frac{a_1}{H}$ is the normalized crack length, and $F_M(\xi)$ is a dimensionless correction function which captures the crack-geometry effects, given by:

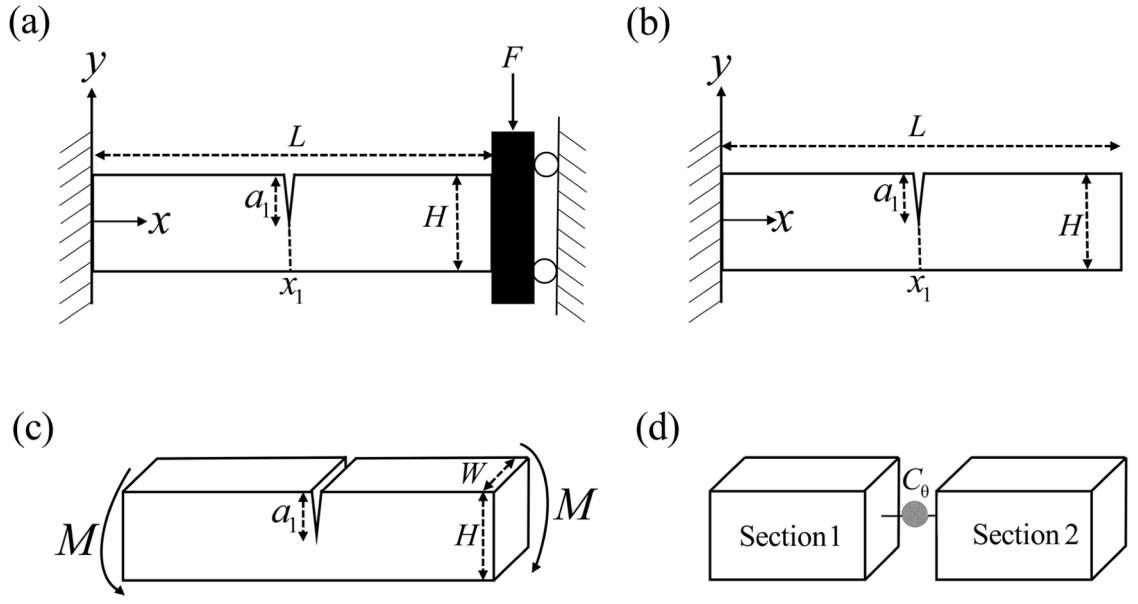

Fig. 1. (a) Fixed–guided cracked nanobeam considered for bending analysis with an applied load F at the guided end. (b) Cantilever cracked nanobeam considered for free vibration analysis. (c) Mode I deformation induced by the bending moment M. (d) Representation of a crack modeled as a rotational elastic spring with compliance C_θ. All nanobeams have a rectangular cross-section with in-plane thickness H, out-of-plane width W, and length L. The cracked nanobeam contains a single edge crack of length a_1 located at position x_1 along the beam.

$$F_M(\xi) = \sqrt{\left(\frac{2}{\pi\xi}\right)\tan\frac{\pi\xi}{2}}\left(\frac{0.923 + 0.199\left(1 - \sin\frac{\pi\xi}{2}\right)^4}{\cos\frac{\pi\xi}{2}}\right). \tag{5}$$

Replacing K_I from Eq. (4) into Eq. (3) results in the following expressions for C_θ:

$$C_\theta = 12\,CH\int_0^\xi R_M^2(\xi)\,d\xi \qquad \text{for} \quad 0 \le \xi \le 0.6$$

$$R_M(\xi) = \sqrt{\tan\frac{\pi\xi}{2}}\left(\frac{0.923 + 0.199\left(1 - \sin\frac{\pi\xi}{2}\right)^4}{\cos\frac{\pi\xi}{2}}\right). \tag{6}$$

$$C_\theta = 2.6535\,CH\int_0^\xi \frac{1}{(1-\xi)^3}\,d\xi \quad \text{for} \quad 0.6 < \xi < 1$$

The foregoing expression for the crack compliance C_θ depends on the normalized crack length ξ as well as on the material properties and the beam geometry. However, because it contains no intrinsic or small-scale parameters, it is unable to capture size effects and therefore is size-independent.

2.2. The SDGE theory

To address the bending and free transverse vibration problems of nanobeams, the SDGE theory is applied within the framework of Euler-Bernoulli beam theory. The original dynamic integral representation of the SDGE model is given by [57]:

$$\frac{\chi(x,t)}{C} = \alpha M(x,t) + (1-\alpha)\int_0^L \phi_{L_C}(x-\zeta)\,M(\zeta,t)\,d\zeta - L_l^2\frac{\partial}{\partial x}\int_0^L \phi_{L_C}(x-\zeta)\,\frac{\partial M(\zeta,t)}{\partial\zeta}d\zeta, \tag{7}$$

where χ and M represent the elastic curvature and bending moment, respectively. The constitutive equation formulated by the SDGE theory includes three nonlocal parameters: the material length scale parameter (L_C), the gradient length scale parameter (L_l), and the mixture parameter (α). Additionally, ϕ_{L_C} is a kernel function which depends on the material length scale parameter L_C and is defined as:

$$\phi_{L_C}(x) = \frac{1}{2L_C}\,e^{\left(-\frac{|x|}{L_C}\right)}. \tag{8}$$

The free transverse vibration problem of small-scale beams with $n-1$ cracks, based on the SDGE theory, was previously solved in [89], with relevant details provided in Appendix A. Incorporating the SDGE theory into the Euler–Bernoulli beam framework yields the following spatial governing differential equations for each segment k of the nanobeam, including $n-1$ cracks:

$$L_C^2\frac{d^6V_k}{dx^6} - \frac{d^4V_k}{dx^4} + CI_2\left(\alpha L_C^2 + L_l^2\right)\omega^2\frac{d^4V_k}{dx^4} - \left(CI_2 + CI_0\left(\alpha L_C^2 + L_l^2\right)\right)\omega^2\frac{d^2V_k}{dx^2} + CI_0\omega^2V_k = 0, \tag{9}$$

for $k = 1, 2, \ldots, n$, where ω is the frequency of vibration, and V is the mode shape.

The system of governing differential equations has the total order of $6n$. Solving this system requires two constitutive boundary conditions, *2 (n-1)* constitutive continuity conditions, 4 variationally consistent boundary conditions, and *4(n-1)* variationally consistent continuity conditions. The full set of governing equations, boundary and continuity conditions, and the solution procedures for both static and dynamic analyses are provided in Appendix A.

For the vibration problem of a cantilever nanobeam containing a single edge crack (see Fig. 1(b)), the system of governing differential equations, together with the required continuity and boundary conditions, results in a homogeneous system of 12 algebraic equations for 12 unknown constants. A non-trivial solution exists only when the determinant of the coefficient matrix vanishes, yielding the characteristic equation for determining the natural frequencies. The roots of this characteristic equation, i.e., the natural frequencies, are then computed numerically using the bisection method.

For the bending problem of a cracked fixed-guided nanobeam (see Fig. 1(a)), the solution is obtained directly from the dynamic formulation by removing all time-dependent terms and imposing the appropriate boundary conditions. For the bending problem of a fixed–guided nanobeam "without" a crack, the following closed-form solution for the bending stiffness is obtained:

$$K_{\text{SDGE}} = \frac{A}{B_1 + B_2 + B_3}, \tag{10}$$

where:

$$\begin{aligned}
A &= \left(((\alpha-1)L_C + L)e^{\frac{L}{L_C}} - (\alpha-1)L_C\right)H^3WE\\
B_1 &= \left(\begin{array}{l}-12(\alpha-1)^2L_C^4 - 12(\alpha-1)^2L_C^3L + \left(-3(\alpha-1)^2L^2 + 12L_l^2 - 12\alpha L_l^2\right)L_C^2\\ +L_l^2(6-6\alpha)LL_C\end{array}\right)e^{-\frac{L}{L_C}}\\
B_2 &= \left(\begin{array}{l}-12(\alpha-1)^2L_C^4 + (12-12\alpha)LL_C^3 + \left(3(\alpha-1)^2L^2 + 12L_l^2 - 12\alpha L_l^2\right)L_C^2\\ +\left(\left(-4+4\alpha\right)L^3 + L_l^2\left(-18+6\alpha\right)L\right)L_C + 6L^2L_l^2 + L^4)\end{array}\right)e^{\frac{L}{L_C}}\\
B_3 &= \left(\begin{array}{l}24(\alpha-1)^2L_C^4 + \left(12\alpha^2 - 12\alpha\right)LL_C^3 + \left((12\alpha-12)L^2 + 24\alpha L_l^2 - 24L_l^2\right)L_C^2\\ +\left((2\alpha-2)L^3 + 12LL_l^2\right)L_C + 6L^2L_l^2\end{array}\right)
\end{aligned} \tag{11}$$

This equation is a function of the nanobeam dimensions and includes three nonlocal parameters, namely L_C, L_l and α.

3. Molecular dynamics simulations

The MD simulations are performed using the Large Scale Atomic/Molecular Massively Parallel Simulator (LAMMPS) [90] to investigate the mechanical behavior of a series of silicon nanobeams with various lengths while maintaining a constant aspect ratio. All nanobeams have a square cross-section with $W = H = L/12$, where the beam length L ranges from 26.07 nm to 182.48 nm. The simulation of the longest beam consists of >2.3 million silicon atoms.

The nanobeams are constructed from single-crystal silicon with a diamond cubic lattice structure and a lattice constant of 0.5431 nm. Unless otherwise stated, the silicon lattice structure is oriented such that the x-axis corresponds to the $[1\ 1\ 1]$ crystallographic direction along the beam length, while the y-axis and z-axis align with the $[\bar{1}\ 2\ \bar{1}]$ and $[\bar{1}\ 0\ 1]$ crystallographic directions, respectively.

In this study, the Stillinger-Weber (SW) potential [91] is employed. The SW potential is particularly suitable for covalently bonded materials with diamond cubic structure, such as silicon, providing both computational efficiency and accuracy for studying the mechanical behavior of silicon structures. The SW potential has been shown to adequately capture key experimentally measured properties related to crystal structure, elasticity, and fracture. For instance, it is reported in [92] that the SW potential predicts a lattice parameter of 0.5431 nm, a C_{11} constant of 162 GPa, and a relaxed {111} shuffle plane surface energy of 1.45 J/m^2, which are in good agreement with the experimentally reported values of 0.5429 nm [92,93], 167 GPa [92,93], and 1.24 J/m^2 [92,94], respectively. In addition, the capability of the SW potential to model fracture-related phenomena in silicon has been demonstrated in the literature. For example, lattice trapping barriers to brittle fracture in silicon have been investigated using the SW potential [92]. Furthermore, the thermodynamic driving forces and activation barriers associated with crack growth, dislocation emission, and amorphization at a crack tip in silicon have been successfully studied using this potential [95].

In the present study, the system remains strictly within the elastic regime, where the mechanical response is governed primarily by bond stretching without bond rupture or crack evolution. The crack is introduced as a pre-existing geometric defect through atomic layer removal and remains stationary throughout the simulations. Under these specific conditions, the SW potential is expected to provide a physically consistent description of atomic interactions in silicon and is therefore well-suited for generating reliable atomistic data. Additionally, the capability of the SW potential to capture the LEFM strain singularity at the crack tip in large nanobeams (L ≈ 180 nm) is demonstrated in Section 4.2.5.

The SW potential presented in Appendix B incorporates both two-body and three-body interactions, enabling the capture of bond stretching and angular interactions. For silicon, the parameters of the SW potential were originally calibrated to reproduce key thermodynamic, structural, and elastic properties, including the equilibrium behavior at 0 K and the melting temperature. The specific parameter values used in this work are listed in Table 1. All parameters without explicit physical dimensions are dimensionless.

The MD simulations are conducted in a 3D domain with non-periodic boundary conditions in all directions, and a time step of 1 fs. After the initial atomic configuration of the nanobeam is created, the system energy is minimized using the conjugate gradient algorithm. The nanobeam is then equilibrated for 100 ps at a temperature of 1 K using the canonical NVT ensemble with a Nose–Hoover thermostat. After equilibration, the nanobeam is prepared for the subsequent mechanical simulations, specifically free transverse vibration and bending analyses.

Both intact and cracked nanobeams are examined. As shown in Fig. B1 in Appendix B, cracks are introduced by deleting a single layer of atoms at the crack location. To evaluate the structural integrity of the introduced crack, a localized Radial Distribution Function (RDF) analysis of the near-tip atoms was conducted (see Fig. B2). Before equilibrium, the RDF shows sharp peaks confirming that every single atom is placed in a perfectly ideal crystalline lattice position. It is the ideally sharp crack scenario assumed by classical Linear Elastic Fracture Mechanics (LEFM). Following equilibration, the perfect preservation of the first nearest-neighbor peak confirms that the primary Si-Si bonds remain unchanged. Simultaneously, an intensity reduction is observed in the second nearest-neighbor peak, due to a slight rearrangement of the atoms at the crack faces to minimize free surface energy. Nevertheless, the crack maintains a sharp geometry, in agreement with the idealized crack representation in continuum fracture mechanics, even after equilibration. As will be shown in Section 4.2.5, cracks introduced via the deletion of a single atomic layer in sufficiently long nanobeams ($L \approx$ 180 nm) successfully capture the classical LEFM near-tip strain singularity.

3.1. MD simulation of free transverse vibration

The free transverse vibration behavior of the silicon cantilever nanobeams is investigated by first establishing a fixed–free configuration. As illustrated in Fig. B1(a) in Appendix B, a region with a length of $0.04L$ at the left end of the nanobeam (labeled "fixed") is fully constrained in all directions throughout the simulation, while the remainder of the nanobeam is allowed to deform.

After energy minimization and thermal equilibration, an excitation is applied to a small region at the free end along the y-axis to initiate vibration. Atoms inside this region are displaced at a prescribed constant velocity in the transverse (y) direction for a short duration. The excitation amplitude (always <2% of the beam length) and velocity were chosen to ensure that the response remains within the elastic regime. An excitation velocity of 0.01 Å/ps was used in the simulations. To ensure that the excitation velocity does not influence the dynamic response, a convergence study was conducted with two smaller velocities (0.001 and 0.005). The derived natural frequencies were identical across all cases, demonstrating that the computed frequencies are independent of the excitation velocity within this range.

This controlled motion generates an initial bent configuration and stores elastic energy in the beam, thereby establishing the initial conditions required for free vibration. During the excitation phase, atoms in the fixed region remain fully constrained, whereas atoms in the middle region are free to move and are maintained at 1 K using an NVT ensemble. Conducting the simulations at 1 K minimizes thermal fluctuations of atoms and ensures a stable and reliable evaluation of the intrinsic mechanical behavior. It also enables the isolation of size-dependent effects without interference from thermal noise.

Once the desired initial deformation is achieved, the prescribed motion is removed, the thermostat is turned off, and the system transitions to the NVE ensemble. The beam then vibrates freely under the influence of its internal elastic forces. Throughout this stage, the average y-coordinate of atoms within the excitation region is recorded at each time step, providing a displacement signal from which the natural frequencies are extracted.

The free transverse vibration simulations are conducted for both intact and cracked beams of various lengths. Very long cracks are

Table 1
Parameter set of the SW potential for silicon, calibrated to reproduce structural and thermodynamic properties [91]. The potential function is presented in Appendix B.

ε (eV)	σ (Å)	a	λ	γ	$\cos\theta_0$	A	B	p	q
2.1683	2.0951	1.80	21.0	1.20	−1/3	7.049556277	0.6022245584	40	0.0

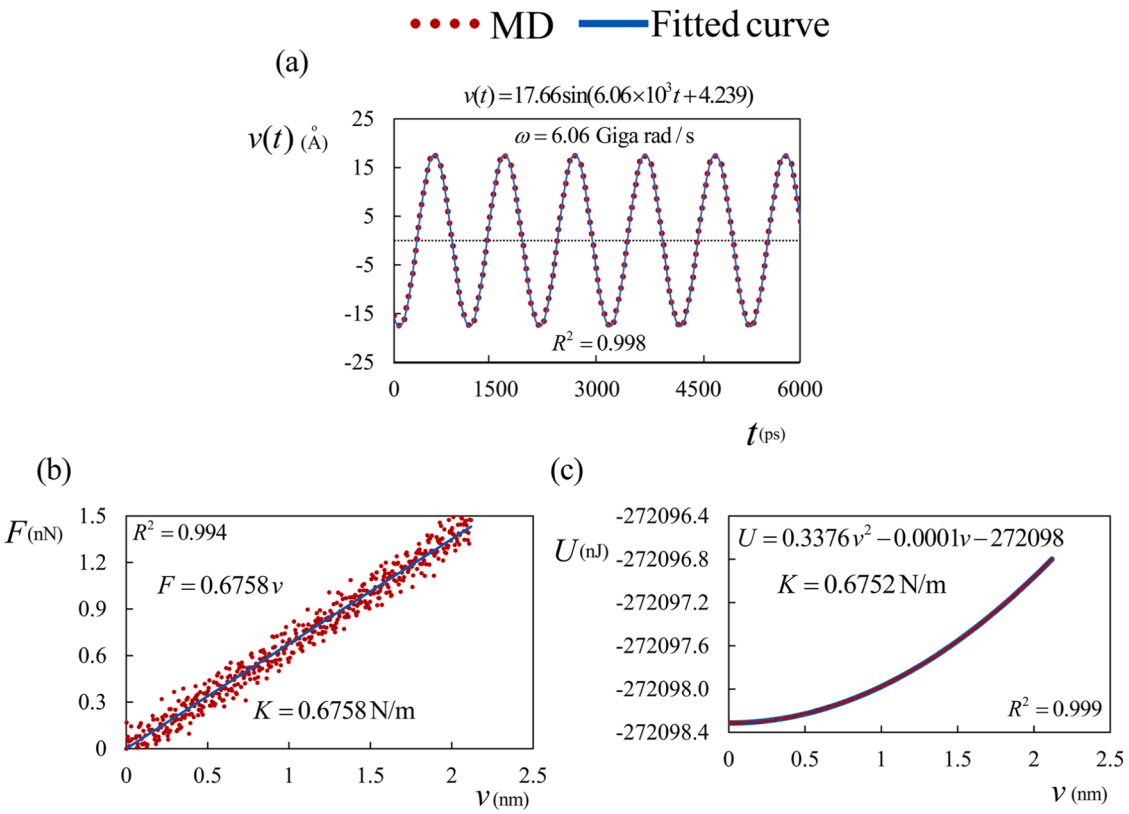

Fig. 2. (a) Extraction of the natural frequency of a cantilever nanobeam from the vibration response obtained in MD simulations, approximated using a sinusoidal function. Determination of the bending stiffness of a fixed–guided nanobeam from MD results based on (b) the load–displacement curve and (c) the potential energy–displacement curve. Both nanobeams have a length $L = 104.28$ nm and an aspect ratio $W = H = L/12$.

avoided to ensure that the crack surfaces remain open throughout the vibration process. The extracted natural frequencies for intact beams are used to calibrate the SDGE model parameters for silicon, while simulations of cracked beams quantify the variation of crack compliance with crack size and beam dimensions.

Fig. 2(a) illustrates how the first natural frequency of a cantilever intact nanobeam of length 104.28 nm is extracted from the MD simulation results by tracking the average y-coordinate of atoms within the excitation region over time t. The recorded vibration response is approximated using a sinusoidal function of the form

$$v(t) = A\sin(Bt + C) \quad \Rightarrow \quad \omega = 10^3 B \quad (\text{Giga} \quad \text{rad/s}), \tag{12}$$

where A, B, and C are curve-fitting parameters, and displacement and time have the dimensions of Å and ps. The natural frequency of the nanobeam is then determined from the fitted parameter B, as $\omega = 10^3 B$, expressed in units of gigaradians per second (Giga rad/s). For the present case, the displacement profile is well captured by the function $17.66\sin\left(6.06\times10^{-3}t + 4.239\right)$. From this fitting, the natural frequency of the nanobeam is determined to be $\omega = 6.06$ Giga rad/s.

To further examine the influence of temperature, additional simulations were performed at $T = 300$K for the natural frequency analysis of intact and cracked nanobeams. The results showed that, within the elastic regime considered in this study, the effect of temperature on the vibrational response is negligible, with differences remaining below 3%, thereby justifying the use of low-temperature simulations in the present analysis.

3.2. MD simulation of bending

Bending simulations are performed on nanobeams with a fixed–guided boundary condition, where the beam is divided into three regions: fixed, middle, and mobile, as shown in Fig. B1(c) in Appendix B. The lengths of the fixed and mobile regions are each equal to $0.04L$. To ensure that the imposed boundary constraints do not influence the extracted mechanical response, a convergence study was performed on the smallest nanobeam considered in this work ($L = 26.07$ nm) by increasing the constrained end length from $0.04L$ to $0.1L$. The extracted bending stiffness changed from $K = 0.13054$ N/m to $K = 0.13001$ N/m, corresponding to a relative difference below 0.3%. This negligible variation confirms that the selected constrained length of $0.04L$ is sufficient to eliminate boundary effects and ensure accurate MD results.

Throughout the deformation process, the temperature is maintained at 1 K using the NVT ensemble. To simulate bending, atoms in the mobile region are displaced at a constant velocity along the y-axis, while their movement in the other directions is constrained. This configuration models the bending of a fixed-guided nanobeam. To ensure a linear elastic response, the maximum displacement applied during the bending simulations is limited to 2.0% of the total beam length.

Following each simulation, the results are processed to determine the bending stiffness of each nanobeam. This bending stiffness can be obtained either using the applied force at the guided end of the nanobeam or the potential energy of the middle region. In the first method, the bending stiffness is calculated as the slope of the load-displacement $(F-\nu)$ curve, as shown in Fig. 2(b). In the second method, as illustrated in Fig. 2(c), it is derived from the relationship between the potential energy (U) of the middle region and the displacement (ν) at the guided end, expressed as follows:

$$K = \frac{d^2U}{d\nu^2}. \tag{13}$$

To assess the reliability of the stiffness extraction procedure, the bending stiffness was evaluated using both the force–displacement method and the potential energy method. The two approaches produced

closely matching results, with differences generally below 3–4% for all considered beam lengths and crack depths. However, the potential energy method consistently yielded higher R^2 values and smoother responses, indicating superior numerical stability. This is because the force–displacement method depends on local reaction forces and is therefore more sensitive to numerical fluctuations, whereas the potential energy method is based on the global energy of the system. Consequently, the stiffness values reported in this study are obtained using the potential energy method. Similar to the free transverse vibration simulations, the bending simulations are performed for both intact and cracked beams of various lengths. The bending stiffness values obtained from the MD simulations of intact nanobeams are used to calibrate the SDGE bending model parameters for silicon, while the simulations of cracked beams are employed to examine the size dependence of crack compliance.

4. Results and discussions

This section explores the existence of size effects on crack compliance in both free transverse vibration and bending problems of cracked silicon nanobeams. First, both SDGE models for bending and free transverse vibration are calibrated using data obtained from MD simulations of intact nanobeams. The calibrated SDGE models are then used to investigate the size dependence of crack compliance by comparing their predictions with the MD simulation results.

It should be noted that the Young's modulus of [111]- and [100]-oriented bulk silicon is taken as 140 GPa and 100.16 GPa, which are close to those predicted by the SW potential [96]. Additionally, the density of silicon is $\rho = 2329$ kg/m^3.

4.1. Calibration of SDGE models

Since the SDGE model involves three nonlocal parameters, it is necessary to determine their values for nanobeams composed of single-crystal silicon. The calibration is performed using MD simulation data for both bending and free transverse vibration of intact nanobeams with varying lengths and a fixed aspect ratio of $W = H = L/12$.

MD simulation results for the first natural frequencies (ω_{MD}) of intact cantilever silicon nanobeams, along with the corresponding predictions from the classical size-independent continuum model (ω_{Loc}) and their ratios, are summarized in Table 2. Similarly, Table 3 presents the MD-derived bending stiffness values (K_{MD}) for intact fixed-guided silicon nanobeams, together with the corresponding classical continuum predictions (K_{Loc}), and their ratios.

In addition, Fig. 3(a) and Fig. 3(b) illustrate the frequency ratios $\left(\frac{\omega_{\mathrm{MD}}}{\omega_{\mathrm{Loc}}}\right)$ for cantilever nanobeams and bending stiffness ratios $\left(\frac{K_{\mathrm{MD}}}{K_{\mathrm{Loc}}}\right)$ for fixed-guided nanobeams versus beam length. The curves clearly reveal pronounced size effects as both ratios are significantly less than one for short beams. For example, the frequency ratio is 0.844, and the bending stiffness ratio is 0.742 for the nanobeam with a length of 26.07 nm. As the beam length increases, these size effects diminish, and the ratios approach unity. For the nanobeam with a length of 182.48 nm, the frequency and bending stiffness ratios reach 0.981 and 0.997, respectively. Therefore, based on the MD results, the length of 182.48 nm may be interpreted as a critical length scale for the present configurations, beyond which size effects become negligible and classical continuum models provide reliable predictions. The critical length is not a universal material constant, but depends on the structural configuration, including beam geometry, aspect ratio, and boundary conditions, as also reported in previous experimental studies [97,98].

Table 2
MD simulation results for the first natural frequencies (ω_{MD}) of intact cantilever nanobeams with varying lengths, along with the corresponding predictions from the classical size-independent continuum model (ω_{Loc}), and their ratios. The intact nanobeams have a square cross-section with dimensions $W = H = L/12$. Young's modulus of [111]-oriented bulk silicon is taken as $E = 140$ GPa.

L (nm)	ω_{MD} (Giga rad/s)	ω_{Loc} (Giga rad/s)	$\frac{\omega_{\mathrm{MD}}}{\omega_{\mathrm{Loc}}}$
26.07	21.24	25.17	0.844
52.14	11.62	12.58	0.924
78.21	7.88	8.39	0.939
104.28	6.06	6.29	0.963
130.34	4.84	5.03	0.962
156.41	4.09	4.19	0.976
182.48	3.52	3.59	0.981

Table 3
MD simulation results for the bending stiffness (K_{MD}) of intact fixed-guided nanobeams with varying lengths, along with the corresponding predictions from the classical size-independent continuum model (K_{Loc}), and their ratio. The intact nanobeams have a square cross-section with dimensions $W = H = L/12$. Young's modulus of [111]-oriented bulk silicon is taken as $E = 140$ GPa.

L (nm)	K_{MD} (N/m)	K_{Loc} (N/m)	$\frac{K_{\mathrm{MD}}}{K_{\mathrm{Loc}}}$
26.07	0.1305	0.1760	0.742
52.14	0.3102	0.3520	0.881
78.21	0.4779	0.5280	0.905
104.28	0.6752	0.7040	0.959
130.34	0.8374	0.8800	0.952
156.41	1.0270	1.0560	0.973
182.48	1.2282	1.2320	0.997

The parameters of the SDGE models are determined using a nonlinear least-squares regression procedure. The MD results for bending stiffness and natural frequencies are assumed to satisfy

$$\mathrm{Y}_{\mathrm{MD}}(L_i) = \mathrm{Y}_{\mathrm{SDGE}}(L_i,\ L_C,\ \alpha,\ L_l) + e_i, \tag{14}$$

where e_i is the residual at each data point, defined as the difference between the SDGE model predictions and the corresponding MD results. Here, Y is the natural frequency for the vibration problem, and the bending stiffness for the bending problem.

The parameter calibration problem is formulated as the minimization of a least-squares objective function $S(L_C, \alpha, L_l)$ as follows:

$$J = \min_{L_C,\alpha,L_l} S(L_C,\alpha,L_l) = \min_{L_C,\alpha,L_l} \frac{\sum_{i=1}^{N}[w_i(\mathrm{Y}_{\mathrm{MD}}(L_i) - \mathrm{Y}_{\mathrm{SDGE}}(L_i,\ L_C,\ \alpha,\ L_l))]^2}{\mathrm{Var}(\mathrm{Y}_{\mathrm{MD}})}. \tag{15}$$

The weights w are assumed to be equal to 5 for the two shortest beams and equal to 1 for the remaining beams. This choice is consistent with the fact that the size effect is more pronounced at smaller length scales, yielding more informative parameter identification. Although this weighting scheme results in a highly accurate calibration, as will be shown in the remainder of this section, other weighting choices could in principle also achieve a similar calibration accuracy.

The denominator normalizes the objective by the variance of the MD data as follows:

$$\mathrm{Var}(\mathrm{Y}_{\mathrm{MD}}) = \frac{1}{N}\sum_{i=1}^{N}\left(\mathrm{Y}_{\mathrm{MD}}(L_i) - \widehat{\mathrm{Y}}_{\mathrm{MD}}\right)^2, \tag{16}$$

where $\widehat{\mathrm{Y}}_{\mathrm{MD}}$ is the mean of the MD dataset. While this normalization does not change the minimization problem since it acts as a constant scaling factor, it makes the objective function dimensionless.

Because the SDGE predictions for bending stiffness and natural frequencies depend nonlinearly on the SDGE model parameters, the minimization problem is solved iteratively. This is performed using the Differential Evolution (DE) algorithm, which minimizes the least-squares objective functions presented in Eq. (15). At each iteration, the behavior of the nonlinear model in the vicinity of the current parameter estimates is used to guide the parameter update to reduce the

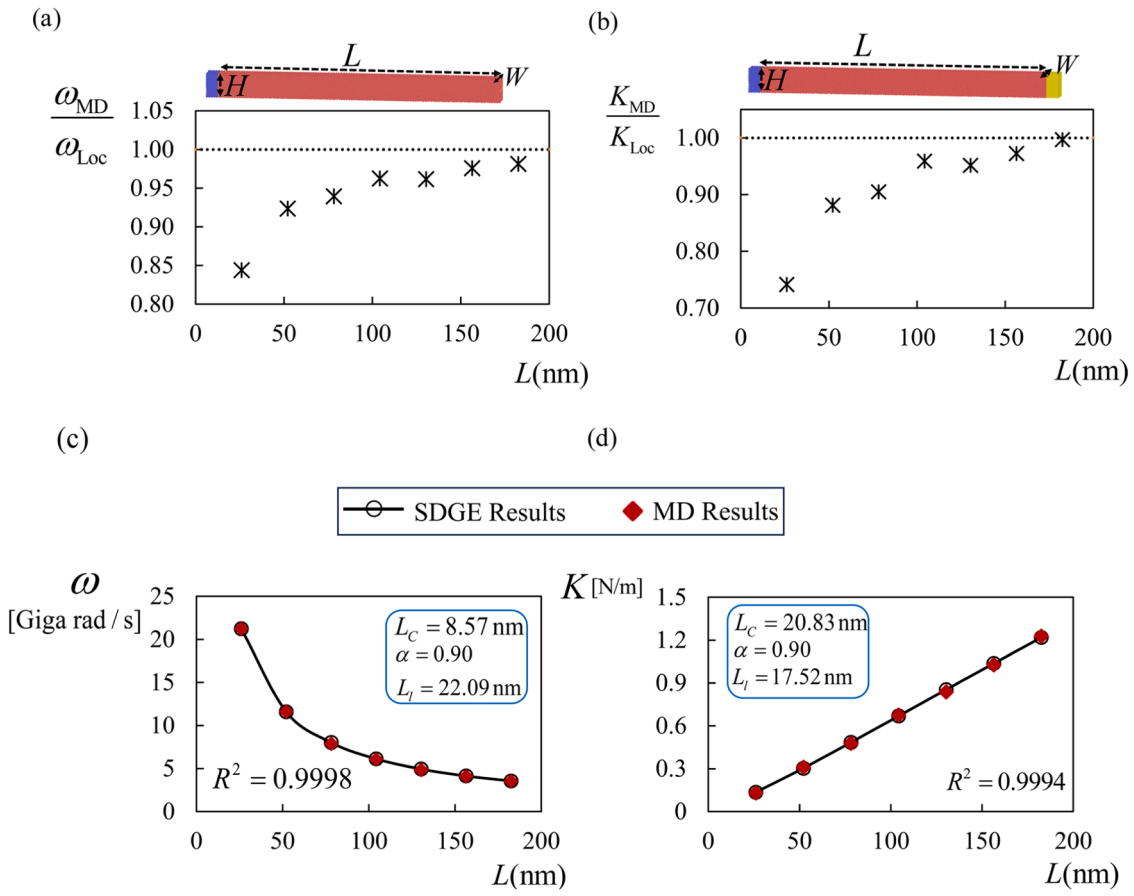

Fig. 3. (a) Ratio of the first natural frequencies of intact cantilever nanobeams obtained from MD simulations (ω_{MD}) to the corresponding predictions of the classical size-independent continuum model (ω_{Loc}) as a function of nanobeam length L. (b) Ratio of the bending stiffness of intact fixed–guided nanobeams obtained from MD simulations (K_{MD}) to the corresponding predictions of the classical size-independent continuum model (K_{Loc}) as a function of nanobeam length L. (c) Calibration of the SDGE model for free transverse vibration of cantilever nanobeams. (d) Calibration of the SDGE model for bending of fixed–guided nanobeams. All nanobeams are made of single-crystal silicon with crystallographic orientation [111] and have a square cross-section with $W = H = L/12$. Young's modulus of [111]-oriented bulk silicon is taken as $E = 140$ GPa.

Table 4
Calibrated nonlocal parameters of the SDGE bending and vibration models based on MD simulation results for nanobeams composed of single-crystal silicon with crystallographic orientation [111]. Nanobeams have a square cross-section with $W = H = L/12$. Young's modulus of [111]-oriented bulk silicon is taken as $E = 140$ GPa.

Problem	L_C (nm)	α	L_l (nm)	R^2	Objective function J
Vibration	8.57	0.90	22.09	0.9998	0.00123
Bending	20.83	0.90	17.52	0.9994	0.00663

least-squares objective function. The iterative process is repeated until successive iterations produce negligible changes in the least-squares objective function. More information about the calibration procedure and stability of the identified parameters is given in Appendix C.

The accuracy of fit is quantified using the coefficient of determination R^2, defined as:

$$R^2 = 1 - \frac{SS_E}{SS_T}, \tag{17}$$

where SS_E is the residual sum of squares andSS_T is the total sum of squares, given by:

$$SS_E = \sum_{i=1}^{N} [Y_{SDGE}(L_i,\ L_C,\ \alpha,\ L_l) - Y_{MD}(L_i)]^2$$
$$SS_T = \sum_{i=1}^{N} [Y_{MD}(L_i) - \overline{Y}_{MD}]^2 \tag{18}$$

A comparison between MD results and the calibrated SDGE model predictions is illustrated in Fig. 3(c) and 3(d) respectively. The resulting calibrated nonlocal parameter values are summarized in Table 4.

Although identical calibration frameworks are employed for both bending and vibration problems, the resulting nonlocal parameters exhibit noticeable differences, particularly in the parameter L_C. These discrepancies primarily arise from the fundamentally different nature of the two mechanical responses. It is well established from both experimental and numerical studies that the magnitude and manifestation of size effects depend on the type of loading applied to nanostructures, such as bending, vibration, tension, or buckling [19,46,99]. For example, experimental investigations on ZnO nanowires have shown that stiffening size effects are significantly more pronounced under buckling compared to tension [100]. Such observations indicate that the effective nonlocal length-scale parameters governing different deformation modes are not necessarily identical. In addition, boundary conditions play a crucial role in determining the mechanical response and associated size effects. Different support configurations (e.g., clamped, simply supported, or free) alter the strain distribution and deformation patterns within the structure, which in turn affects the calibration of

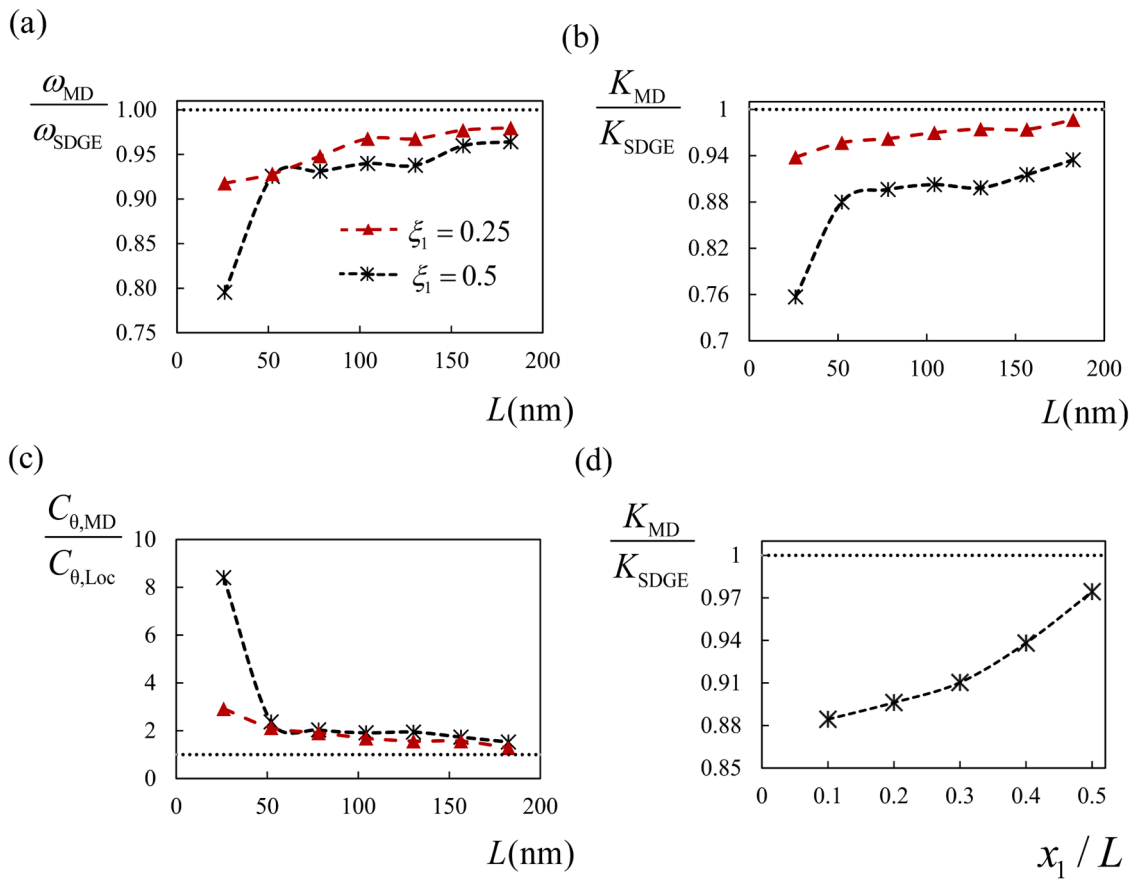

Fig. 4. (a) Ratios of the natural frequencies of cracked cantilever nanobeams obtained from MD simulations (ω_{MD}) to those predicted by the calibrated SDGE model (ω_{SDGE}) as a function of nanobeam length. (b) Ratios of the bending stiffness of cracked fixed–guided nanobeams obtained from MD simulations (K_{MD}) to those predicted by the calibrated SDGE model (K_{SDGE}) as a function of nanobeam length. (c) Ratio of crack compliance of cracked fixed–guided nanobeams obtained from MD simulations of the bending problem ($C_{\theta,MD}$) to predictions of the size-independent model ($C_{\theta,Loc}$) [88] as a function of nanobeam length. (d) Ratios of bending stiffness of cracked fixed–guided nanobeams obtained from MD simulations (K_{MD}) to those predicted by the calibrated SDGE model (K_{SDGE}) versus dimensionless crack location x_1/L for a fixed–guided nanobeam with length $L = 78.21$ nm and crack length $a_1 = 0.5H$. (a)–(c) All nanobeams have a square cross-section with $W = H = L/12$ and a single edge crack located at $x_1 = 0.2L$ with crack lengths $a_1 = 0.25H$ and $0.5H$. All nanobeams are made of single-crystal silicon with crystallographic orientation [111]. Young's modulus of [111]-oriented bulk silicon is taken as $E = 140$ GPa.

nonlocal parameters.

4.2. Size dependence of crack compliance

4.2.1. Vibration problem

Using the calibrated nonlocal parameters, the SDGE vibration model is applied to examine the influence of size effects on crack compliance in free transverse vibration of cantilever nanobeams containing an edge crack. The natural frequencies of cracked nanobeams with varying lengths and a fixed aspect ratio of $W = H = L/12$ are computed using the calibrated SDGE model and compared with the corresponding MD simulation results to assess whether the crack compliance exhibits size dependency. Nanobeams with a single edge crack located at $x_1 = 0.2\,L$ are considered, with crack lengths of $a_1 = 0.25\,H$ and $a_1 = 0.5\,H$. Movie S1 in the Supplementary Materials demonstrates the free transverse vibration response of the silicon beam with a length of 104.28 nm and a crack length of $0.5H$

It is important to note that, at the cracked cross-section, the crack compliance of each rotational spring C_θ is evaluated using the closed-form expressions provided in Eq. (6). This expression, which is based on classical fracture mechanics within the framework of local elasticity, does not include any size effects. Thus, any deviation between the results of MD simulations and the calibrated SDGE vibration model for cracked nanobeams reflects the size effect on the crack compliance that is not captured by the classical expression in Eq. (6).

Fig. 4(a) illustrates the ratios of the MD-predicted natural frequencies to the SDGE predictions for cracked nanobeams. For shorter beams and a crack length of $a_1 = 0.5\,H$, the MD-predicted frequencies are significantly lower than the SDGE results, consistent with the size-dependent softening behavior previously observed in intact beams. In this case, however, the discrepancy arises from size effects in the crack compliance. For example, the ratio is 0.795 for a nanocantilever of length 26.07 nm. As the nanobeam length increases, the size effect on crack compliance diminishes, and the MD results converge toward the calibrated SDGE predictions, with the ratio reaching 0.964 for a length of 182.28 nm.

For nanobeams containing a crack of length $a_1 = 0.25\,H$, the size effect on crack compliance is less pronounced than that for $a_1 = 0.5\,H$; nevertheless, the same trend is observed. The ratio increases from 0.918 for a nanocantilever of length 26.07 nm to 0.980 for a nanobeam of length 182.28 nm.

These observations demonstrate that crack compliance in nanobeams is size-dependent and cannot be accurately captured using classical formulas derived from local fracture mechanics, Eq. (6). The MD simulations reveal that cracks introduce greater flexibility at small scales than predicted by size-independent models. As the nanobeam length grows, these effects become less dominant, and the classical expression becomes effectively valid in the limit of large lengths.

4.2.2. Bending problem

Similar to the vibration problem, the calibrated SDGE bending model is employed to predict the bending stiffness of fixed–guided cracked nanobeams with varying lengths, and the results are compared with MD simulations to assess the size dependence of crack compliance. Since a size-independent formula is used to calculate crack compliance (C_θ) within the SDGE model framework, the discrepancy between the MD simulation results and those obtained from the calibrated SDGE bending model is attributed to the size effects in crack compliance.

Fixed–guided silicon nanobeams containing a single edge crack located at $x_1 = 0.2\,L$ are analyzed for two crack lengths, $a_1 = 0.25\,H$ and $a_1 = 0.5\,H$. The comparative results of MD simulations and the calibrated SDGE bending model for cracked silicon nanobeams are presented in Fig. 4(b). The comparison involves calculating the ratios of bending stiffness values obtained from MD simulations (K_{MD}) to those predicted by the calibrated SDGE model (K_{SDGE}). Movie S2 in the Supplementary Materials demonstrates the bending response of the silicon beam with a length of 104.28 nm and a crack length of $0.5H$

As shown in Fig. 4(b), a significant discrepancy is observed between the MD-derived bending stiffness values (K_{MD}) and those predicted by the calibrated SDGE model (K_{SDGE}) for the nanobeams with a crack length $a_1 = 0.5\,H$, particularly for shorter nanobeams. For example, for a nanobeam with $L = 26.07$ nm, the ratio $\frac{K_{\mathrm{MD}}}{K_{\mathrm{SDGE}}}$ is 0.756, indicating a pronounced size effect associated with crack compliance. Consistent with the trends observed in the vibration analysis, this discrepancy decreases as the nanobeam length increases, and the ratio $\frac{K_{\mathrm{MD}}}{K_{\mathrm{SDGE}}}$ gradually approaches unity, demonstrating that the size effect on crack compliance diminishes for longer beams.

For nanobeams containing a shorter crack of $a_1 = 0.25\,H$, the size effect is less pronounced. In this case, the ratio $\frac{K_{\mathrm{MD}}}{K_{\mathrm{SDGE}}}$ is 0.938 for $L = 26.07$ nm, reflecting reduced size sensitivity due to the smaller crack length. Nevertheless, the same trend is observed, with the ratio approaching unity as the nanobeam length increases, indicating the gradual reduction of size effects on crack compliance.

Moreover, the MD simulation results are used to determine the crack compliance values $\left(C_{\theta,\,\mathrm{MD}}\right)$, which are compared with those obtained from the size-independent formulation $\left(C_{\theta,\,\mathrm{Loc}}\right)$ given in Eq. (6). This is achieved by substituting the bending stiffness values derived from MD simulations into the SDGE model and calculating the corresponding crack compliance that results in this bending stiffness. Similar to the trend observed in the curve of bending stiffness ratios, Fig. 4(c) clearly shows that the size effect on crack compliance is significantly more pronounced in shorter nanobeams. For example, for the nanobeam with $L = 26.07$ nm and a crack of length $a_1 = 0.5\,H$, the ratio $\frac{C_{\theta,\mathrm{MD}}}{C_{\theta,\mathrm{Loc}}}$ is 8.404. This size effect diminishes as the crack length decreases; for the same nanobeam with $a_1 = 0.25\,H$, the ratio is reduced to 2.916.

To investigate the influence of crack location and its interaction with size effects, MD simulations are performed for different crack positions $x_1 = 0.1L, 0.2L, 0.3L, 0.4L, 0.5L$. The resulting bending stiffness values K_{MD} are compared with the corresponding predictions of the calibrated SDGE model. The results for a fixed–guided nanobeam with length $L = 78.21$ nm and crack length $a_1 = 0.5H$, shown in Fig. 4(d), indicate that the deviation between MD and SDGE model predictions is more pronounced when the crack is located near the clamped end. This behavior arises because the bending stiffness is significantly higher near the clamped boundary, which amplifies the influence of the crack on the structural response (see Eq. (1)).

Specifically, when the crack is located at $x_1 = 0.1L$, the ratio $\frac{K_{\mathrm{MD}}}{K_{\mathrm{SDGE}}}$ is approximately 0.88. As the crack moves away from the clamped end, this ratio increases, reaching approximately 0.97 at $x_1 = 0.5L$, indicating improved agreement between the SDGE model and MD simulations in regions of lower bending stiffness.

The bending analysis further confirms that crack compliance is size-dependent, which is not captured by classical local models. At small scales, MD simulations reveal greater flexibility than predicted by size-independent models. With increasing beam length, the influence of these nanoscale effects on crack compliance diminishes, and the classical formulation becomes progressively more accurate.

Table 5
MD simulation results for the bending stiffness (K_{MD}) of intact fixed-guided silicon nanobeams with varying lengths, along with the corresponding predictions from the classical size-independent continuum model (K_{Loc}), and their ratio. The intact nanobeams have a square cross-section with dimensions $W = H = L/12$. Young's modulus of [100]-oriented bulk silicon is taken as $E = 100.16$ GPa [96].

L (nm)	K_{MD} (N/m)	K_{Loc} (N/m)	$\frac{K_{\mathrm{MD}}}{K_{\mathrm{Loc}}}$
26.07	0.100	0.126	0.799
52.14	0.239	0.251	0.952
78.21	0.365	0.377	0.969
104.28	0.491	0.503	0.977
130.34	0.619	0.629	0.985
156.41	0.745	0.754	0.988
182.48	0.868	0.880	0.987

4.2.3. Effect of crystallographic orientation

To examine the influence of crystallographic orientation on the size dependence of crack compliance, additional bending simulations are performed for both intact and cracked silicon nanobeams oriented along the [100] direction. The geometric configuration of the nanobeams and cracks is identical to that considered for the [111] orientation, namely fixed–guided nanobeams with a square cross-section ($W = H = L/12$) containing a single edge crack located at $x_1 = 0.2L$ with crack length $a_1 = 0.5H$.

The MD simulation results for intact [100]-oriented silicon nanobeams, together with the corresponding predictions from classical continuum mechanics, are presented in Table 5. The Young's modulus for [100]-oriented bulk silicon is taken as $E = 100.16$ GPa [96].

The variation of the bending stiffness ratio $\frac{K_{\mathrm{MD}}}{K_{\mathrm{Loc}}}$, shown in Fig. 5(a), exhibits a clear size-dependent trend similar to that observed for the [111] orientation. The size effect is most pronounced for shorter nanobeams and gradually diminishes with increasing beam length. For example, the ratio increases from 0.799 at $L = 26.07$ nm to 0.987 at $L = 182.48$ nm, approaching unity as the beam length increases.

Subsequently, the MD-derived bending stiffness values are used to calibrate the SDGE model. The calibration process, illustrated in Fig. 5 (b), yielded a set of nonlocal parameters for the [100]-oriented bending problem as follows:

$$L_C = 20.88\,\mathrm{nm},\ \alpha = 0.9,\ L_l = 17.23\,\mathrm{nm}.$$

The calibrated SDGE model is then employed to predict the response of cracked nanobeams. A comparison between MD simulations and SDGE model predictions for [100]-oriented nanobeams with a single edge crack is presented in Fig. 5(c). Similar to the [111] case, a noticeable discrepancy is observed for shorter nanobeams. For instance, at $L = 26.07$ nm, the ratio $\frac{K_{\mathrm{MD}}}{K_{\mathrm{SDGE}}}$ is 0.794, indicating a pronounced size effect associated with crack compliance. This ratio gradually increases with beam length, reaching 0.977 at $L = 182.48$ nm, demonstrating the reduction of size effects in longer beams.

In addition, the crack compliance values obtained from MD simulations for [100]-oriented silicon nanobeams $\left(C_{\theta,\,\mathrm{MD}}\right)$ are compared with those predicted by the classical size-independent formulation $\left(C_{\theta,\mathrm{Loc}}\right)$ given in Eq. (6). As shown in Fig. 6(d), the size effect on crack compliance is significantly more pronounced for shorter nanobeams. For example, at $L = 26.07$ nm with $a_1 = 0.5H$, the ratio $\frac{C_{\theta,\mathrm{MD}}}{C_{\theta,\mathrm{Loc}}}$ is 7.624. As the beam length increases, this ratio decreases and approaches unity.

Overall, the results exhibit trends consistent with those observed for the [111] orientation, particularly in terms of the size-dependent

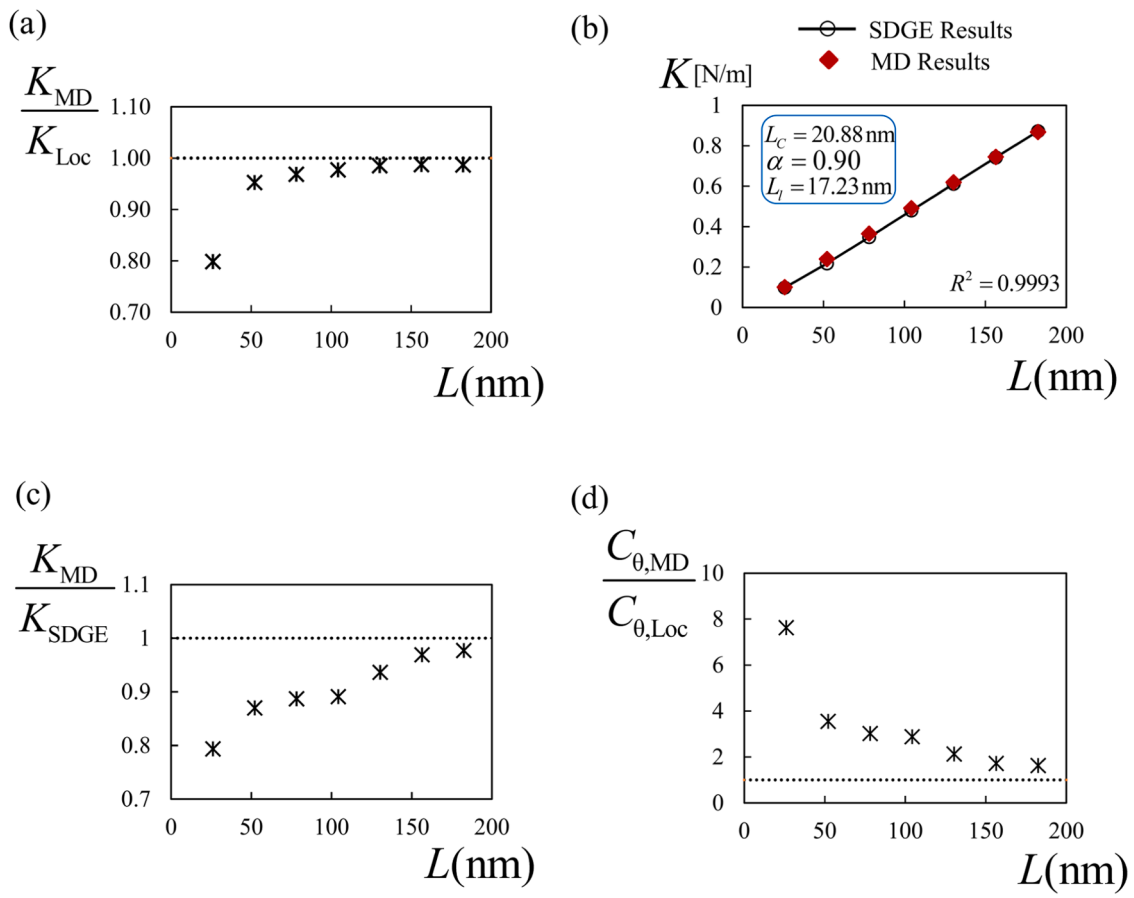

Fig. 5. (a) Ratio of the bending stiffness of intact fixed–guided nanobeams obtained from MD simulations (K_{MD}) to the corresponding predictions of the classical size-independent continuum model (K_{Loc}) as a function of nanobeam length L. (b) Calibration of the SDGE model for bending of intact fixed–guided nanobeams using the MD simulation results. (c) Ratios of the bending stiffness of fixed–guided nanobeams containing a single edge crack of length $a_1 = 0.5H$ located at $x_1 = 0.2L$, obtained from MD simulations (K_{MD}) to those predicted by the calibrated SDGE model (K_{SDGE}) as a function of nanobeam length. (d) Ratio of crack compliance of fixed–guided nanobeams containing a single edge crack of length $a_1 = 0.5H$ located at $x_1 = 0.2L$, obtained from MD simulations ($C_{\theta,MD}$) to predictions of the size-independent model [88] ($C_{\theta,Loc}$) as a function of nanobeam length. All nanobeams are made of single-crystal silicon with crystallographic orientation [100] and have a square cross-section with $W = H = L/12$. The Young's modulus of [100]-oriented bulk silicon is taken as $E = 100.16$ GPa [96].

variation of crack compliance. This confirms that the identified size effects and the corresponding conclusions are not limited to a specific crystallographic direction. Therefore, the selection of the [111] orientation in the primary analysis is representative and does not restrict the generality of the results.

4.2.4. *Effect of boundary conditions*

To examine the influence of boundary conditions on the size dependence of crack compliance, the bending response of silicon nanobeams with clamped–clamped boundary conditions is investigated. MD simulations are performed for both intact and cracked silicon nanobeams with crystallographic orientation [111]. The geometric configuration is identical to that considered for the fixed–guided case, namely nanobeams with a square cross-section ($W = H = L/12$). The cracked nanobeams contain a single edge crack located at $x_1 = 0.2L$ with crack length $a_1 = 0.5H$, as shown in Fig. 6(a).

As illustrated in Fig. 6(a), the nanobeam is divided into four regions: two fixed regions at both ends, a middle region, and a mobile region. The fixed regions, each with a length of $0.04L$, represent clamped boundaries where all degrees of freedom are constrained. The mobile region, located at the midspan of the beam, consists of a layer of atoms used to apply displacement with a constant velocity along the y-direction, while constraining their motion in the remaining directions. All other MD simulation details are consistent with those used for the fixed–guided nanobeams. The bending stiffness of the clamped–clamped nanobeam is calculated by dividing the reaction load by the midspan deflection. The results of MD simulations, the corresponding predictions from the classical size-independent continuum model (K_{Loc}), and their ratios are reported in Table 6.

The results in Table 6, also shown in Fig. 6(b), reveal a clear size-dependent behavior in the bending stiffness of clamped–clamped silicon nanobeams. For all beam lengths, the MD-derived stiffness values K_{MD} are consistently lower than the corresponding classical predictions K_{Loc}, indicating that the classical continuum model overestimates the stiffness at the nanoscale for silicon nanobeams. This discrepancy is most pronounced for shorter nanobeams, where the ratio $\frac{K_{MD}}{K_{Loc}}$ is as low as 0.662 at $L = 26.07$ nm. As the beam length increases, this ratio gradually approaches unity, reaching 0.899 at $L = 182.48$ nm. This trend demonstrates that size effects diminish with increasing structural length, and the predictions of classical continuum mechanics become progressively more accurate.

A further observation is that size effects in nanobeams with clamped–clamped boundary conditions are more pronounced than in fixed–guided nanobeams. For example, for the shortest nanobeam at $L = 26.07$ nm, the stiffness ratio is 0.662 for the clamped–clamped case, whereas it is 0.742 for the fixed–guided case. Similarly, for the longest beam at $L = 182.48$ nm, the fixed–guided configuration yields a ratio of 0.997, indicating that size effects are essentially negligible, while the clamped–clamped case still shows a value of 0.899, demonstrating that size effect persists even at larger lengths.

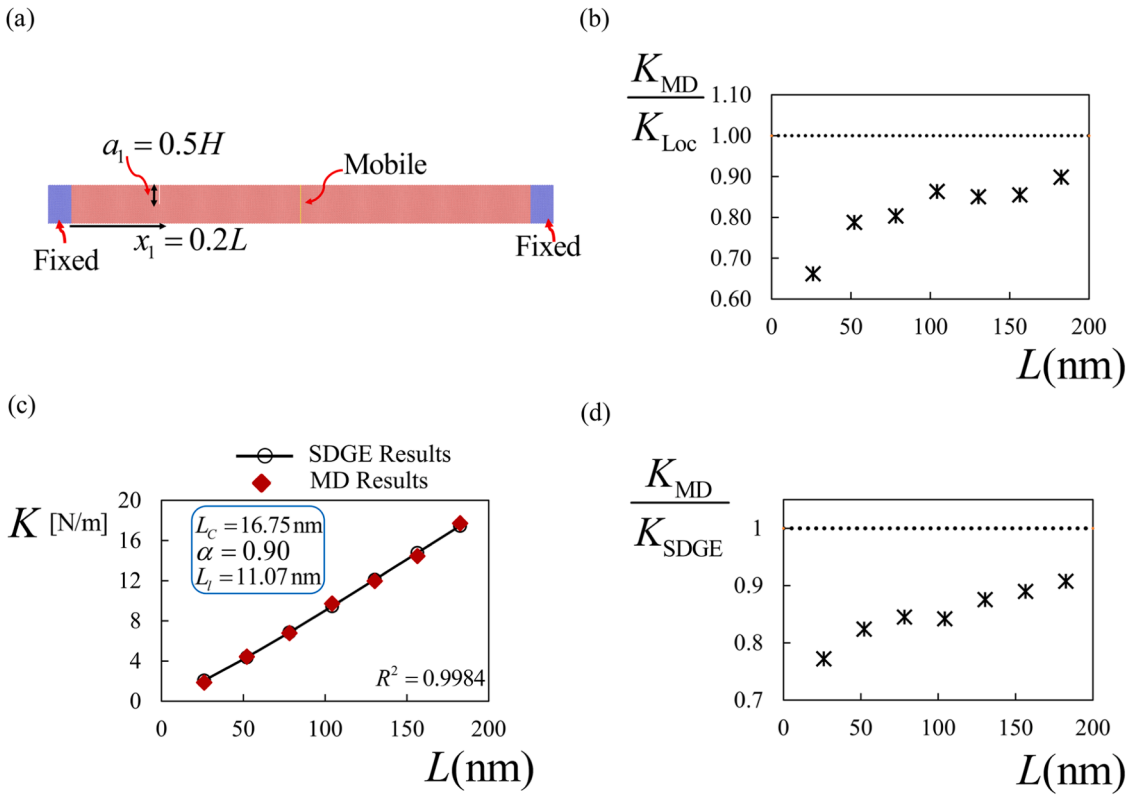

Fig. 6. (a) Schematic of a cracked silicon nanobeam containing a single edge crack of length $a_1 = 0.5H$ located at $x_1 = 0.2L$, used in MD simulations of bending for clamped–clamped boundary conditions. (b) Ratio of the bending stiffness of intact clamped-clamped nanobeams obtained from MD simulations (K_{MD}) to the corresponding predictions of the classical size-independent continuum model (K_{Loc}) as a function of nanobeam length L. (c) Calibration of the SDGE model for bending of intact clamped-clamped nanobeams using the MD simulation results. (d) Ratios of the bending stiffness of clamped–clamped nanobeams containing a single edge crack of length $a_1 = 0.5H$ located at $x_1 = 0.2L$, obtained from MD simulations (K_{MD}) to those predicted by the calibrated SDGE model (K_{SDGE}) as a function of nanobeam length. All nanobeams are made of single-crystal silicon with crystallographic orientation [111] and have a square cross-section with $W = H = L/12$. The Young's modulus of [111]-oriented bulk silicon is taken as $E = 140$ GPa.

Table 6
MD simulation results for the bending stiffness (K_{MD}) of intact clamped–clamped silicon nanobeams with varying length, together with the corresponding predictions from the classical size-independent continuum model (K_{Loc}), and their ratios. All nanobeams have a square cross-section with dimensions $W = H = L/12$ and crystallographic orientation [111]. Young's modulus of [111]-oriented bulk silicon is taken as $E = 140$ GPa.

L (nm)	K_{MD} (N/m)	K_{Loc} (N/m)	$\frac{K_{MD}}{K_{Loc}}$
26.07	1.864	2.816	0.662
52.14	4.436	5.632	0.788
78.21	6.788	8.448	0.803
104.28	9.725	11.264	0.863
130.34	11.975	14.080	0.850
156.41	14.447	16.896	0.855
182.48	17.712	19.713	0.899

This difference in the influence of boundary conditions is reflected in the calibrated nonlocal parameters shown in Fig. 6(c). The calibration process using MD simulation results for clamped–clamped nanobeams yields the following values of the nonlocal parameters:

$$L_C = 16.75\,\text{nm},\ \alpha = 0.9,\ L_l = 11.07\,\text{nm}.$$

The significant differences in the values of L_C, and in particular L_l, highlight the impact of boundary conditions on the calibrated nonlocal parameters and, consequently, on size-dependent mechanical behavior at the nanoscale.

Finally, by comparing the predictions of the calibrated SDGE model for the bending of clamped–clamped silicon nanobeams with the corresponding values obtained from MD simulations for nanobeams containing a single edge crack located at $x_1 = 0.2L$ with crack length $a_1 = 0.5H$, it can be understood that the crack compliance is size-dependent. This is reflected in Fig. 6(d). As shown, a significant difference exists between the MD-derived bending stiffness values (K_{MD}) and those predicted by the calibrated SDGE model (K_{SDGE}) for shorter nanobeams. For the shortest nanobeam with $L = 26.07$ nm, the ratio $\frac{K_{MD}}{K_{SDGE}}$ is 0.772, while for the longest nanobeam, $L = 182.48$ nm, this ratio increases to 0.901, approaching unity. Consistent with the trends observed in the previous cases, this discrepancy decreases with increasing nanobeam length, demonstrating that size effects in crack compliance diminish for longer beams. The reason for this discrepancy between MD simulation results and the calibrated SDGE bending predictions is the use of a size-independent formulation for calculating crack compliance (C_θ) within the SDGE model framework, which does not capture size-dependent effects.

4.2.5. *Crack tip strain analysis*

So far, it has been demonstrated that the classical formulation presented in Eq. (6) fails to predict the crack compliance of shorter nanobeams adequately. This divergence from classical Linear Elastic Fracture Mechanics (LEFM) implies that the local crack-tip fields should also deviate from continuum predictions. Specifically, under macroscopic conditions, the axial strain ahead of a Mode I crack tip is governed by a $r^{-1/2}$ singularity. Therefore, it can be concluded that if the macroscopic compliance equations fail at the nanoscale, the underlying local strain singularity must also break down. This deviation is explicitly captured and evaluated in Fig. 7.

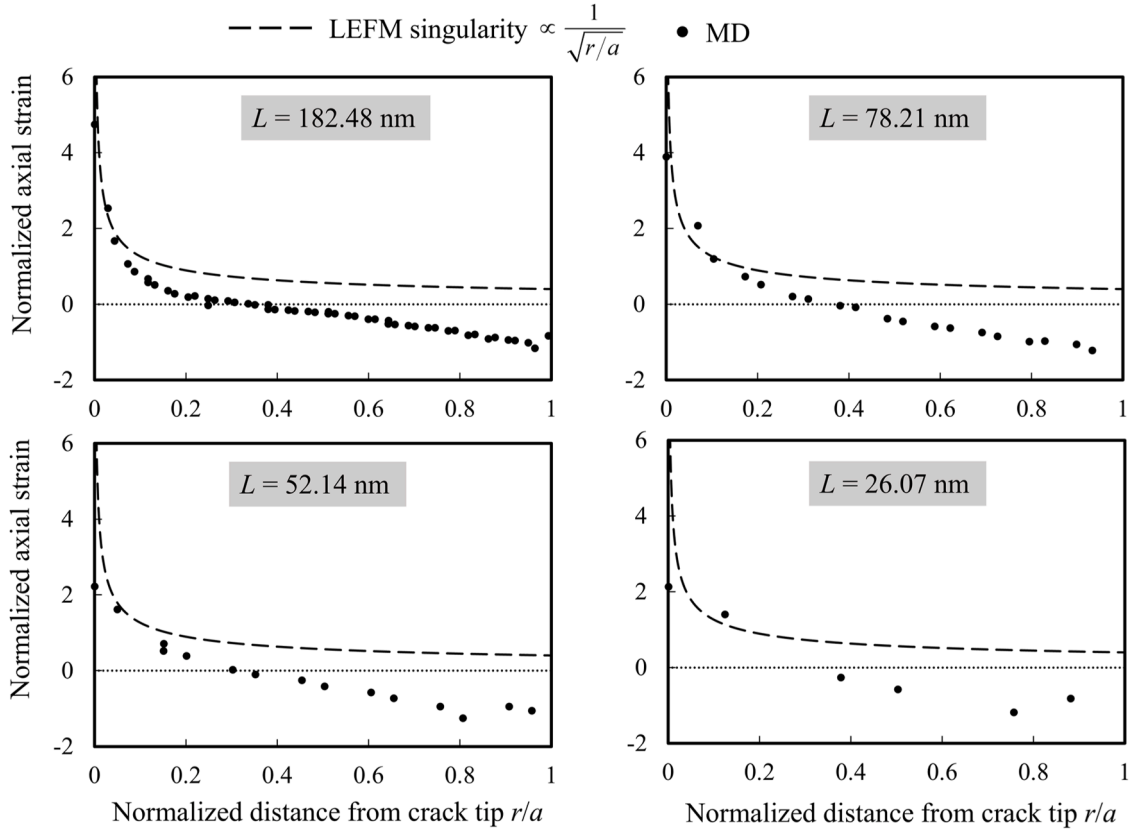

Fig. 7. Normalized axial strain ahead of the crack tip plotted against the normalized distance from the tip (r/a) for different fixed-guided nanobeams with $L = 182.48$ nm, 78.21 nm, 52.14 nm, and 26.07 nm subjected to 0.02 L displacement. The axial strains are normalized using the absolute value of the compressive strain measured at the opposite surface of the beam, farthest from the crack tip. All nanobeams have a square cross-section with $W = H = L/12$ and one crack located at $x_1 = 0.2L$ with a crack length of $0.5H$. All nanobeams are made of single-crystal silicon with crystallographic orientation [111].

For the longest silicon nanobeam ($L = 182.48$ nm), the classical $r^{-1/2}$ singularity in the vicinity of the crack tip is preserved in MD results, although the normalized axial strain takes a finite, positive dimensionless value of 4.74 at the crack tip. This physically realistic, finite strain at the crack tip aligns with previous MD simulations, where finite crack-tip stresses were similarly observed in silica fracture specimens [101]. As the distance from the crack tip increases, the dominance of the singular field rapidly decays, and the strain profile transitions to follow a linear distribution dictated by the global bending moment acting on the cross-section. This observation validates the capability of our MD simulations to capture classical continuum fracture mechanics when the nanobeam is sufficiently large. This localized continuum convergence explains the agreement observed in Fig. 4(c) between the MD-derived compliance and the classical continuum predictions for the nanobeam with $L = 182.48$ nm.

As the nanobeam length decreases, the maximum axial strain at the crack tip is significantly reduced. For instance, the normalized axial strain at the crack tip drops from 4.74 in the longest beam to just 2.13 in the shortest. Furthermore, the number of atoms within the remaining uncracked ligament diminishes, making the discrete nature of the lattice increasingly prominent. In the shortest beam, this ligament consists of only a few atomic layers, making the continuum assumption invalid. Consequently, the MD results deviate significantly from the analytical LEFM strain field. This profound deviation from theoretical continuum predictions explains the significant divergence in crack compliance between the classical formulation and our MD results, as observed in Fig. 4(c).

5. Limitations and future outlook

The work presented here demonstrates that the size-independent crack compliance formula, commonly used in nanobeam formulations, must be revisited to account for nanoscale size effects. While this study represents a first step, it has several limitations that guide future research directions:

- An explicit formula should be developed to replace the existing size-independent one. This is challenging because the size effect is a multi-factor phenomenon, influenced by crack length, boundary conditions, and the nature of the applied structural load (e.g., bending, vibration, or buckling).
- This study investigates silicon nanobeams, which exhibit a softening response at smaller scales and an accompanying increase in crack compliance. Conversely, materials that stiffen at the nanoscale are expected to exhibit reduced crack compliance. Additionally, because the intensity of the size effect varies across materials, any explicit size-dependent formula for crack compliance must be material-dependent.
- We have studied slender nanobeams, where the bending moment dominates deformation, and shear effects can be neglected. Consequently, the crack is modeled solely as a rotational spring. For shorter nanobeams, shear deformation becomes significant, requiring the introduction of an additional translational spring at the cracked cross-section. The size dependence of this translational compliance, which is related to Mode II crack sliding deformation, remains an open question for future study.

Future experimental investigations may follow the same logic

developed in this study. Focusing on silicon, due to its high relevance in MEMS and NEMS applications, nanocantilevers of varying sizes but identical aspect ratios can be fabricated from a silicon wafer using the Focused Ion Beam (FIB) technique. The bending stiffnesses can first be determined for crack-free beams using in situ scanning electron microscopy nanoindentation techniques. This provides the necessary data to calibrate an appropriate nonclassical continuum model (analogous to the SDGE theory calibration in this study). Subsequently, FIB can be used to mill precise pre-cracks into the nanocantilevers, allowing for the determination of the bending stiffnesses of the cracked structures. By combining these experimental results with the calibrated nonclassical formulations, one can empirically define size-dependent crack compliances.

Through systematic testing of samples with different crack lengths and locations, curve-fitting techniques can yield an experimentally validated formula for silicon nanobeams in bending. Similar free transverse vibration tests using atomic force microscopy can be used to establish equivalent formulations for dynamic responses. Such an experimental campaign is currently underway, and those findings will be communicated in future articles.

6. Conclusions

This study investigated the influence of size effects on crack compliance in silicon nanobeams by combining large-scale MD simulations involving >2.3 million atoms with the local/nonlocal stress-driven gradient elasticity (SDGE) model. Both bending and free transverse vibration analyses were performed for nanobeams containing a single edge crack.

The SDGE model was first calibrated using MD results for intact nanobeams. It was found that the calibrated nonlocal parameters are not universal constants, but depend on both the boundary conditions and the type of mechanical problem. In particular, different parameter sets are required for bending and vibration analyses, and their values vary among cantilever, fixed–guided, and clamped–clamped configurations, highlighting the need for case-specific calibration.

The calibrated framework was then applied to cracked nanobeams over a wide range of lengths. The results show a pronounced size dependence of crack compliance, with MD simulations predicting significantly higher crack-induced flexibility than classical size-independent formulations for short nanobeams. This discrepancy becomes more pronounced for smaller beam lengths and larger crack sizes, and gradually decreases as the beam length increases.

The convergence toward classical behavior was also assessed. The results show that the rate of convergence depends on the structural configuration. For cantilever and fixed–guided nanobeams, the discrepancy between MD results and classical predictions falls below approximately 2% at lengths around 182 nm, indicating that classical models provide sufficiently accurate predictions beyond this scale. In contrast, for clamped–clamped nanobeams, size effects persist at this length for both the overall mechanical response and crack compliance, indicating that a larger length is required for convergence. Therefore, the length beyond which classical behavior is recovered is not universal, but depends on the boundary conditions of the structure. Additional analyses show that the observed trends are consistent across different crystallographic orientations, while boundary conditions affect the magnitude of the size effect, with clamped–clamped nanobeams exhibiting stronger deviations.

Furthermore, an atomic-scale analysis of the axial strain distribution ahead of the crack was conducted for fixed-guided nanobeams of varying lengths. Our analysis demonstrated that for sufficiently long nanobeams ($L \approx 180$ nm), the singular form predicted by LEFM is successfully recovered near the crack tip, although the strain is regularized to a finite value at the crack tip. In contrast, the near-tip axial strain field in short nanobeams deviates from this singular variation, which explains the observed discrepancy in crack compliance between our MD results and the classical LEFM formulation.

Overall, the findings show that classical crack compliance models are inadequate for nanoscale applications. Accurate and reliable crack detection in nanostructures requires models that explicitly incorporate size-dependent effects at cracked cross-sections. Such enhanced models are essential for advancing the structural health monitoring and design of nanoscale devices, including MEMS and NEMS.

A promising direction for future research is the development of fully size-dependent formulations for crack compliance that can be directly incorporated into nonclassical continuum models, eliminating the need for classical approximations. Further extensions to different materials, crack configurations, and loading conditions would broaden the applicability of the proposed framework.

Funding

The financial support provided by the National Science Centre (NCN) in Poland through the grant agreement No: UMO-2022/47/D/ST8/01348 is gratefully acknowledged.

CRediT authorship contribution statement

Akbar Hassanpour: Writing – review & editing, Writing – original draft, Visualization, Validation, Methodology, Investigation, Formal analysis, Data curation. **Hossein Darban:** Writing – review & editing, Supervision, Software, Resources, Project administration, Methodology, Investigation, Funding acquisition, Formal analysis, Conceptualization, Data curation, Validation, Visualization, Writing – original draft.

Declaration of competing interest

The authors declare that they have no known competing financial interests or personal relationships that could have appeared to influence the work reported in this paper.

Acknowledgment

We would like to express our sincere gratitude to Professor Michał Basista from the Institute of Fundamental Technological Research, Polish Academy of Sciences, for his insightful discussions and constructive feedback during the revision process. We gratefully acknowledge the Polish high-performance computing infrastructure PLGrid (HPC Centers: WCSS, ACK Cyfronet AGH) for providing computer facilities and support within the computational grant no PLG/2026/01929.

Supplementary materials

Supplementary material associated with this article can be found, in the online version, at doi:10.1016/j.ijmecsci.2026.111894.

Appendix A: Nonlocal models

Considering an Euler–Bernoulli beam containing $n-1$ discontinuities (such as cracks or concentrated loads) which divide the beam into n segments, the integral representation of the constitutive law in Eq. (7) can be equivalently expressed in differential form for sub-beam k as follows:

$$\chi_k - L_C^2 \frac{\delta^2 \chi_k}{\delta x^2} = C M_k - C\left(\alpha L_C^2 + L_l^2\right) \frac{\delta^2 M_k}{\delta x^2}, \tag{A.1}$$

for $k = 1, 2, \ldots, n$, where n denotes the total number of beam segments.

The transformation of the integral form of the constitutive law in Eq. (7) into the differential form in Eq. (A.1) yields the following constitutive boundary conditions [102]:

$$L_C^2 \frac{\delta^3 \nu_1(x,t)}{\delta x^3} - L_C \frac{\delta^2 \nu_1(x,t)}{\delta x^2} + C\alpha L_C M_1(x,t) - C\left(\alpha L_C^2 + L_l^2\right) \frac{\delta M_1(x,t)}{\delta x} = 0 \qquad \text{at } x = 0, \tag{A.2}$$

$$L_C^2 \frac{\delta^3 \nu_n(x,t)}{\delta x^3} + L_C \frac{\delta^2 \nu_n(x,t)}{\delta x^2} - C\alpha L_C M_n(x,t) - C\left(\alpha L_C^2 + L_l^2\right) \frac{\delta M_n(x,t)}{\delta x} = 0 \qquad \text{at } x = L. \tag{A.3}$$

In addition, at locations of discontinuities such as cracks or concentrated loads, constitutive continuity conditions are required to ensure a well-posed solution of the governing differential equations. These conditions are given by [102]:

$$\begin{aligned}
&L_C^2 \frac{\delta^3 \nu_k(x,t)}{\delta x^3} - L_C \frac{\delta^2 \nu_k(x,t)}{\delta x^2} = -C\alpha L_C M_k(x,t) + C\alpha L_C^2 \frac{\delta M_k(x,t)}{\delta x} \\
&-C(1-\alpha)\left[\sum_{i=1}^{k-1} \int_{x_{i-1}}^{x_i} e^{-\frac{x-\zeta}{L_C}} M_i(\zeta,t)\, d\zeta\right] \qquad \text{at } x = x_{k-1} \\
&+CL_l^2\left[\frac{\delta}{\delta x}\sum_{i=1}^{k-1} \int_{x_{i-1}}^{x_i} e^{-\frac{x-\zeta}{L_C}} \frac{\delta M_i(\zeta,t)}{\delta \zeta}\, d\zeta + \frac{\delta}{\delta x}\int_{x_{k-1}}^{x} e^{-\frac{x-\zeta}{L_C}} \frac{\delta M_k(\zeta,t)}{\delta \zeta}\, d\zeta\right] = 0
\end{aligned} \tag{A.4}$$

and,

$$\begin{aligned}
&L_C^2 \frac{\delta^3 \nu_k(x,t)}{\delta x^3} + L_C \frac{\delta^2 \nu_k(x,t)}{\delta x^2} = C\alpha L_C M_k(x,t) + C\alpha L_C^2 \frac{\delta M_k(x,t)}{\delta x} \\
&+C(1-\alpha)\left[\sum_{i=k+1}^{n} \int_{x_{i-1}}^{x_i} e^{\frac{x-\zeta}{L_C}} M_i(\zeta,t)\, d\zeta\right] \qquad \text{at } x = x_k \\
&-CL_l^2\left[\frac{\delta}{\delta x}\int_{x}^{x_k} e^{\frac{x-\zeta}{L_C}} \frac{\delta M_k(\zeta,t)}{\delta \zeta}\, d\zeta + \frac{\delta}{\delta x}\sum_{i=k+1}^{n} \int_{x_{i-1}}^{x_i} e^{\frac{x-\zeta}{L_C}} \frac{\delta M_i(\zeta,t)}{\delta \zeta}\, d\zeta\right] = 0
\end{aligned} \tag{A.5}$$

According to the Euler-Bernoulli beam theory, the relationship between transverse displacement $v(x,t)$, cross-section rotation $\theta(x,t)$ and the elastic curvature of the beam $\chi(x,t)$ are as follows:

$$\theta_k(x,t) = \frac{\partial \nu_k(x,t)}{\partial x}, \tag{A.6}$$

$$\chi_k(x,t) = \frac{\partial \theta_k(x,t)}{\partial x}. \tag{A.7}$$

Accordingly:

$$\chi_k(x,t) = \frac{\partial^2 \nu_k(x,t)}{\partial x^2}, \tag{A.8}$$

for $k = 1, 2, \ldots, n$.

The dynamic equilibrium equations for the free transverse vibration of sub-beam k based on the Euler-Bernoulli beam model are:

$$\frac{\partial Q_k(x,t)}{\partial x} = -I_0 \ddot{\nu}_k(x,t), \tag{A.9}$$

$$\frac{\partial M_k(x,t)}{\partial x} - Q_k(x,t) = I_2 \ddot{\theta}_k(x,t). \tag{A.10}$$

Where Q and M are shear force and bending moment, respectively. In addition, $\ddot{\nu}_k$ and $\ddot{\theta}_k$ represent the second derivative of ν_k and θ_k with respect to time.

Substituting Eq. (A.10) into Eq. (A.9) gives:

$$\frac{\partial^2 M_k(x,t)}{\partial x^2} - I_2 \frac{\partial^2 \ddot{\nu}_k(x,t)}{\partial x^2} + I_0 \ddot{\nu}_k(x,t) = 0. \tag{A.11}$$

By incorporating Eq. (A.1) into the Euler–Bernoulli beam theory and using Eq. (A.11), the governing differential equation for the dynamic behavior of the nanobeam is obtained as follows:

$$L_C^2\frac{\delta^6 v_k}{\delta x^6} - \frac{\delta^4 v_k}{\delta x^4} - CI_2\left(\alpha L_C^2 + L_l^2\right)\frac{\delta^4 \ddot{v}_k}{\delta x^4} + \left(CI_2 + CI_0\left(\alpha L_C^2 + L_l^2\right)\right)\frac{\delta^2 \ddot{v}_k}{\delta x^2} - CI_0\ddot{v}_k = 0, \tag{A.12}$$

for $k = 1, 2, \ldots, n$.

Additionally, the equations for the bending moment (M) and shear force (Q) are derived as follows:

$$\begin{aligned} M_k &= \frac{1}{C}\left(\frac{\delta^2 v_k}{\delta x^2} - L_C^2\frac{\delta^4 v_k}{\delta x^4}\right) + I_2\left(\alpha L_C^2 + L_l^2\right)\frac{\delta^2 \ddot{v}_k}{\delta x^2} - I_0\left(\alpha L_C^2 + L_l^2\right)\ddot{v}_k \\ Q_k &= \frac{1}{C}\left(\frac{\delta^3 v_k}{\delta x^3} - L_C^2\frac{\delta^5 v_k}{\delta x^5}\right) + I_2\left(\alpha L_C^2 + L_l^2\right)\frac{\delta^3 \ddot{v}_k}{\delta x^3} - \left(I_0\left(\alpha L_C^2 + L_l^2\right) - I_2\right)\frac{\delta \ddot{v}_k}{\delta x} \end{aligned}. \tag{A.13}$$

A.1 Free Transverse Vibration Problem

To solve the governing differential equations in (A.12) for the free transverse vibration of an Euler-Bernoulli nanobeam containing a single edge crack ($n = 2$), the displacement function is separated into a harmonic time-dependent component and a spatial function. Assuming a harmonic response, the displacements can be expressed as:

$$\begin{aligned} \nu_k(x,t) &= e^{i\omega t}V_k(x) \\ \theta_k(x,t) &= e^{i\omega t}\Phi_k(x) \end{aligned}, \tag{A.14}$$

where ω is the frequency.

Substituting Eq. (A.14) into the governing differential Eq. (A.12), results in the following spatial form of governing equation:

$$L_C^2\frac{d^6 V_k}{dx^6} - \frac{d^4 V_k}{dx^4} + CI_2\left(\alpha L_C^2 + L_l^2\right)\omega^2\frac{d^4 V_k}{dx^4} - \left(CI_2 + CI_0\left(\alpha L_C^2 + L_l^2\right)\right)\omega^2\frac{d^2 V_k}{dx^2} + CI_0\omega^2 V_k = 0, \tag{A.15}$$

for $k = 1$ and 2.

In general, the governing differential Eq. (A.15) for a nanobeam containing a single crack is a twelfth-order equation; therefore, its general solution involves 12 unknown constants. These constants are determined by imposing a total of twelve boundary and continuity conditions. Among these, two correspond to the constitutive boundary conditions given in Eqs. (A.2) and (A.3), and two are the constitutive continuity conditions specified in Eqs. (A.4) and (A.5).

In addition, four variationally consistent continuity conditions at each cracked cross-section are given by:

$$\begin{aligned} M_1 &= M_2 \\ Q_1 &= Q_2 \qquad\qquad \text{at } x = x_1 \\ V_1 &= V_2 \\ \frac{dV_2}{dx} - \frac{dV_1}{dx} &= C_\theta M_1 \end{aligned}. \tag{A.16}$$

Finally, four variationally consistent boundary conditions for a cantilever beam are expressed as

$$\begin{aligned} V_1 &= 0 \qquad\qquad \text{at } x = 0 \\ \frac{dV_1}{dx} &= 0 \qquad\qquad \text{at } x = 0 \\ Q_2 &= 0 \qquad\qquad \text{at } x = L \\ M_2 &= 0 \qquad\qquad \text{at } x = L \end{aligned}. \tag{A.17}$$

Applying all boundary and continuity conditions yields a homogeneous system of 12 algebraic equations for the unknown constants, which can be expressed in matrix form. A nontrivial solution exists only when the determinant of the coefficient matrix vanishes. In the present study, the bisection method is employed to find the first root of the determinant of the coefficient matrix, corresponding to the fundamental natural frequency. Further details on the numerical solution procedure for analyzing the free transverse vibration of small-scale beams using the SDGE model can be found in [89].

A.2 Bending Problem

For the bending problem, the solution is obtained directly from the dynamic formulation by setting all time-dependent terms to zero. Applying this reduction to Eq. (A.12) yields the governing differential equation for the static bending response of the nanobeam, expressed as:

$$L_C^2\frac{d^6 v_k}{dx^6} - \frac{d^4 v_k}{dx^4} = 0. \tag{A.18}$$

For the bending of a small-scale beam with fixed–guided boundary conditions and a crack located at x_1, subjected to a concentrated load F at the fixed–guided end, the nanobeam is divided into two segments *($n = 2$)*; hence, $k = 1, 2$. Similar to the free transverse vibration problem, solving the differential Eq. (A.18) governing the bending behavior of the nanobeam requires 12 boundary and continuity conditions. Among these, two are the constitutive boundary conditions given in Eqs. (A.2) and (A.3), and two are the continuity conditions expressed in Eqs. (A.4) and (A.5). In addition, four variationally consistent continuity conditions at each cracked cross-section are provided in Eq. (A.16).

The corresponding variationally consistent boundary conditions for a fixed-guided nanobeam are given below:

$$\begin{aligned} &\nu_1 = 0 && \text{at } x = 0 \\ &\frac{d\nu_1}{dx} = 0 && \text{at } x = 0 \\ &Q_2 = F && \text{at } x = L \\ &\frac{d\nu_2}{dx} = 0 && \text{at } x = L \end{aligned} \quad . \tag{A.19}$$

Applying these conditions yields a system of 12 algebraic equations for the unknown constants. Once the constants are obtained, the displacement field along the nanobeam is fully defined.

It should be noted that the bending stiffness of the fixed–guided nanobeam is defined as:

$$K = \frac{F}{\nu_2(x = L)}. \tag{A.20}$$

For the bending of a small-scale beam with clamped-clamped boundary conditions and a crack located at x_1, subjected to a concentrated load F at the midspan $(x_2 = L/2)$, the nanobeam is divided into three segments *($n = 3$)*; hence, $k = 1, 2, 3$. Therefore, the system of governing differential equations is of order 18, solving it requires 18 boundary and continuity conditions.

The constitutive boundary conditions are the same as those given in Eqs. (A.2) and (A.3). In addition, since two discontinuities exist (at x_1 and x_2) four constitutive continuity conditions are obtained from Eqs. (A.4) and (A.5), applied at x_1 and x_2 for $k = 1, 2, 3$.

Furthermore, four variationally consistent continuity conditions are imposed at each discontinuity, corresponding to the crack location x_1 and the load location x_2:

$$\begin{aligned} &M_1 = M_2 \\ &Q_1 = Q_2 && \text{at } x = x_1 \\ &V_1 = V_2 \\ &\frac{dV_2}{dx} - \frac{dV_1}{dx} = C_\theta M_1 \end{aligned} \quad , \tag{A.21}$$

and,

$$\begin{aligned} &M_2 = M_3 \\ &Q_2 = Q_3 + F && \text{at } x = x_2 \\ &V_2 = V_3 \\ &\frac{dV_2}{dx} = \frac{dV_3}{dx} \end{aligned} \quad . \tag{A.22}$$

Finally, the variationally consistent boundary conditions for a clamped–clamped nanobeam are specified below:

$$\begin{aligned} &\nu_1 = 0 && \text{at } x = 0 \\ &\frac{d\nu_1}{dx} = 0 && \text{at } x = 0 \\ &\nu_3 = 0 && \text{at } x = L \\ &\frac{d\nu_3}{dx} = 0 && \text{at } x = L \end{aligned} \quad . \tag{A.23}$$

The resulting system of equations is solved to obtain the displacement field along the nanobeam.

For a clamped–clamped nanobeam with a point load F applied at midspan, the bending stiffness is expressed as:

$$K = \frac{F}{\nu_2(x = 0.5L)}. \tag{A.24}$$

A1.3 Verification of SDGE Models

Fig. A1 illustrates the predictions of the developed SDGE models for the effect of a crack on the vibrational and bending responses of a silicon nanobeam. The results show the variation in natural frequency and bending stiffness of a silicon nanobeam with a length of $L = 26.07$ nm as a function of dimensionless crack length (a_1/H).

The values of the nonlocal parameters considered in this analysis are those derived from the calibration of the SDGE models using MD simulation results for the free transverse vibration of cantilever nanobeams and the bending of fixed-guided nanobeams made of silicon with crystallographic orientation [111]. These values are $L_C = 8.57$ nm, $\alpha = 0.9$, and $L_l = 22.09$ nm for the vibration problem, and $L_C = 20.83$ nm, $\alpha = 0.9$, and $L_l = 17.52$ nm for the bending problem.

As can be seen from Fig. A1, the calibrated SDGE models for both problems accurately capture the frequency and bending stiffness obtained from MD simulations of the intact nanobeam $(a_1/H = 0)$. In this case, the natural frequency and bending stiffness have their maximum values of 21.242 Giga rad/s and 0.135 N/m, respectively.

In addition, both curves show that as the crack length increases, both the natural frequency and bending stiffness decrease. For the deepest crack with $a_1/H = 0.6$, these values reduce to 15.828 Giga rad/s and 0.104 N/m, respectively. This reduction is attributed to the increase in local flexibility introduced by the crack, which weakens the structural stiffness.

Overall, the results demonstrate that crack length has a significant impact on both stiffness and vibrational characteristics, with larger cracks leading to a substantial impact on the structural performance. This trend is consistently captured by the SDGE models, confirming their capability to represent the effect of geometric discontinuities on the mechanical behavior of nanobeams.

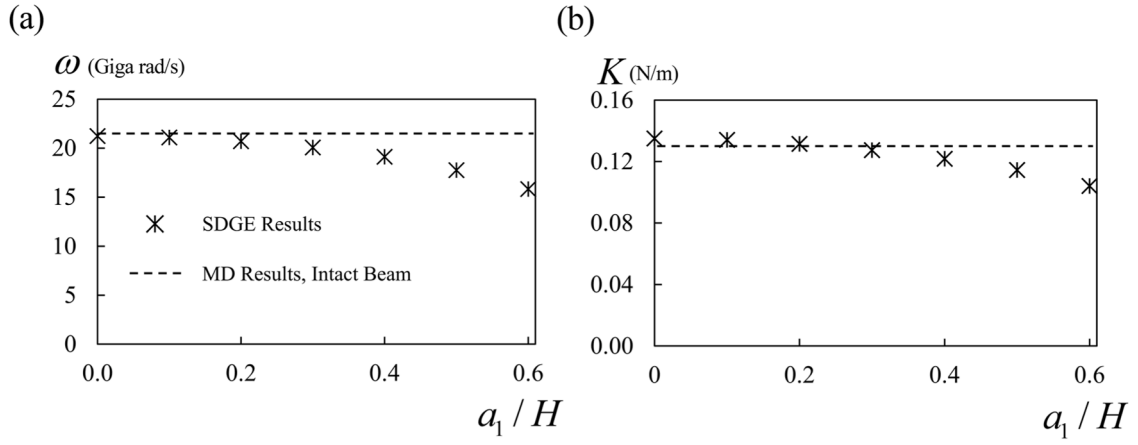

Fig. A1. (a) Predictions of the SDGE model for the natural frequency of a silicon cantilever nanobeam with length $L = 26.07$ nm, as a function of the dimensionless crack length (a_1/H). The nonlocal parameters correspond to those calibrated using MD results for free transverse vibration of cantilever nanobeams, namely $L_C = 8.57$ nm, $\alpha = 0.9$, and $L_l = 22.09$ nm. (b) Predictions of the SDGE model for the bending stiffness of a fixed–guided silicon nanobeam with length $L = 26.07$ nm, as a function of the dimensionless crack length (a_1/H). The nonlocal parameters correspond to those calibrated using MD results for bending of nanobeams, namely $L_C = 20.83$ nm, $\alpha = 0.9$, and $L_l = 17.52$ nm. All nanobeams have a square cross-section with dimensions $W = H = L/12$, crystallographic orientation [111], and contain a single edge crack located at $x_1 = 0.2L$.

Appendix B: The SW Potential, Initial Atomic Configurations, and RDF Diagrams

The total energy E_{SW} is calculated as a sum of two-body ϕ_2 and three-body ϕ_3 interaction terms:
Fig. B1 and Fig. B2

$$E_{SW} = \sum_i \sum_{j>i} \phi_2(r_{ij}) + \sum_i \sum_{j\neq i} \sum_{k>j} \phi_3(r_{ij}, r_{ik}, \theta_{ijk}), \tag{B.1}$$

where:

$$\phi_2(r_{ij}) = A\varepsilon\left[B\left(\frac{\sigma}{r_{ij}}\right)^p - \left(\frac{\sigma}{r_{ij}}\right)^q\right]\exp\left(\frac{1}{r_{ij}/\sigma - a}\right)$$
$$\phi_3(r_{ij}, r_{ik}, \theta_{ijk}) = \lambda\varepsilon\left(\cos\theta_{ijk} - \cos\theta_0\right)^2 \exp\left(\frac{\gamma}{r_{ij}/\sigma - a}\right)\exp\left(\frac{\gamma}{r_{ik}/\sigma - a}\right) \tag{B.2}$$

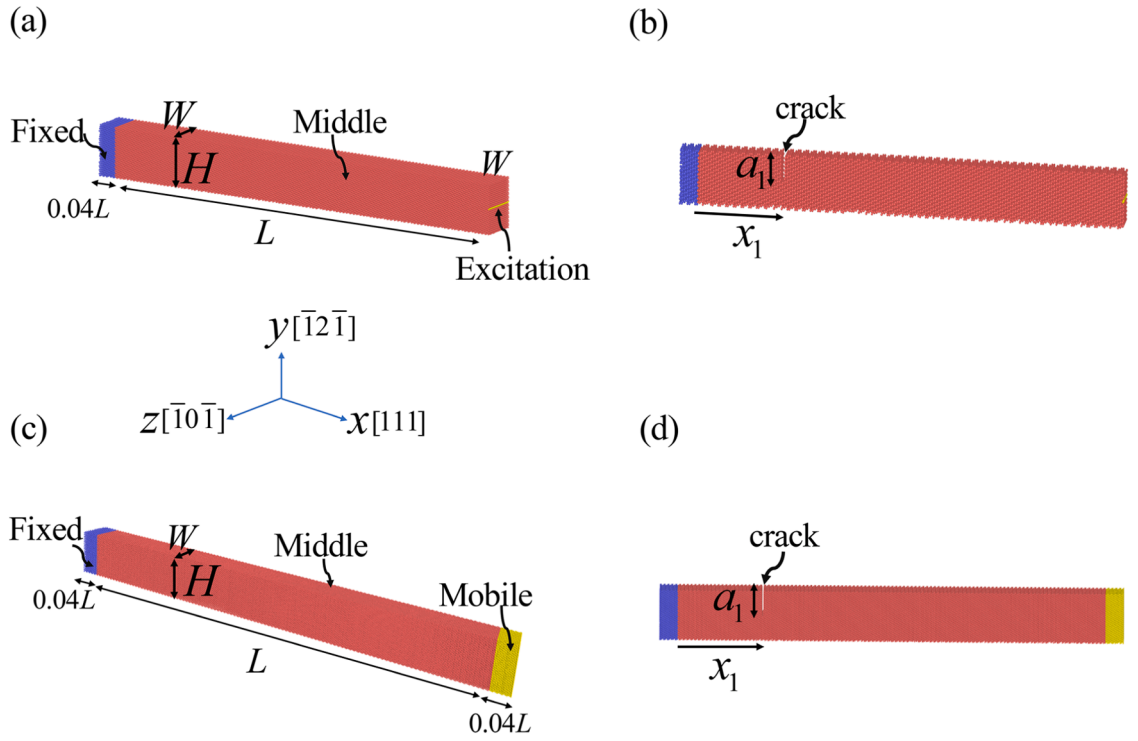

Fig. B1. Schematic of silicon nanobeams used in MD simulations. (a) Intact cantilever nanobeam for free transverse vibration analysis. (b) Cantilever nanobeam containing a crack of length a_1 located at x_1, used for free transverse vibration analysis. (c) Fixed–guided intact nanobeam used for bending simulations. (d) Fixed–guided nanobeam containing a crack of length a_1 located at x_1, used for bending simulations. All nanobeams have a square cross-section with $W = H = L/12$.

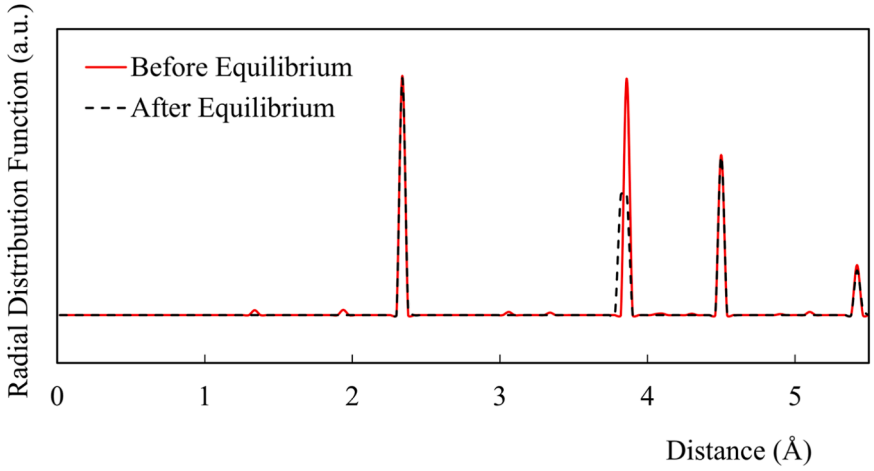

Fig. B2. Localized Radial Distribution Function (RDF) of the atomic configuration near the crack tip before and after thermal relaxation. The analysis was conducted within a cylindrical domain with a radius of 1 nm centered at the crack tip. The nanobeam has a square cross-section with dimensions $W = H = L/12$, crystallographic orientation [111], and contains a single edge crack located at $x_1 = 0.2L$. Results correspond to the $L = 182.48$ nm and a crack length equal to $H/2$.

Appendix C: Parameter Calibration

The characteristic length scales L_C and L_l are constrained within the range [0,25] nm, which is consistent with the geometric dimensions of the nanobeams considered in this study (beam lengths ranging from approximately 26 nm to 182 nm). The mixture parameter α is restricted to the interval [0.2, 0.9] to keep both local and nonlocal contributions in the formulation. For $\alpha = 0$, the local contribution (the first term on the right-hand side of the constitutive Eq. (7)) vanishes, resulting in a fully nonlocal response within the SDGE model. Conversely, as α approaches 1, the nonlocal contribution (the second term on the right-hand side of the constitutive Eq. (7)) diminishes, and the local contribution becomes increasingly dominant.

It is noted that the calibrated values of α consistently converge toward the upper bound of the admissible range. This is because the optimization tends to reduce the nonlocal contribution as it produces a stiffening effect in contrast to the softening effect observed in MD results.

To further assess the stability of the calibrated SDGE parameters, a multi-start global optimization approach is employed, consisting of 30 independent runs initialized with different random seeds. The dispersion of the resulting parameter sets is quantified using the coefficient of variation (CoV), defined as the ratio of the standard deviation to the mean value, expressed in percentage form. The CoV provides a normalized measure of sensitivity to initial conditions and is used here to evaluate the stability of the calibration procedure. A low CoV indicates that the optimization consistently converges to nearly identical solutions regardless of the random initialization of the Differential Evolution (DE) population, while a high

CoV would indicate the presence of multiple competing minima.

Table C.1 summarizes the CoV of the calibrated SDGE parameters. The results show that all calibrated parameters exhibit very low CoV values in both bending and vibration cases. In all cases, CoV remains below 1.1 percent, indicating that the DE algorithm consistently converges to nearly identical solutions across different random initial populations. The smallest variability is observed for the parameter α, suggesting that it is the most strongly constrained parameter by the MD data. Slightly higher CoV values for L_C compared to the other parameters indicate a relatively higher but still very low sensitivity to initialization, which is expected due to its direct role in governing nonlocal length scale effects.

Table C.1
Coefficient of variation (CoV, %) of calibrated SDGE parameters obtained from 30 independent differential evolution runs, quantifying convergence robustness and parameter stability.

Problem	$\mathbf{CoV}_{L_C}$ (%)	$\mathbf{CoV}_{\alpha}$ (%)	$\mathbf{CoV}_{L_l}$ (%)
Vibration	0.31	0.03	0.17
Bending	1.07	0.01	0.63

A local sensitivity analysis is also performed by perturbing the calibrated parameters around their optimal values while keeping the remaining parameters fixed. The analysis focuses on the characteristic length L_C, which exhibits the most pronounced variation between bending and vibration problems.

The sensitivity analysis was conducted by varying L_C by $\pm 5\%$ and $\pm 10\%$ from its calibrated value. The corresponding variations in the objective function for both bending and vibration problems are summarized in Table C.2

Table C.2
Sensitivity of the objective function to perturbations in L_C.

Problem	Perturbation in $\boldsymbol{L_C}$ (%)	Objective function $\boldsymbol{J}$	Relative increase (%)
Bending	−10	0.011713	76.76
Bending	−5	0.007848	18.44
Bending	5	0.007710	16.36
Bending	10	0.010824	63.34
Vibration	−10	0.023383	1809.70
Vibration	−5	0.006529	432.92
Vibration	5	0.006157	402.63
Vibration	10	0.020107	1541.00

The minimum values of the objective function obtained from the calibration procedure are $J_{\min} = 0.00663$ for the bending problem and $J_{\min} = 0.00123$ for the vibration problem. Based on these values, the relative increase in the objective function due to perturbations in L_C is evaluated, as shown in Table C.2.

For the bending problem, a $\pm$ 5% variation in L_C leads to an increase of approximately 16–18% in the objective function, while a $\pm$ 10% perturbation results in a larger increase of about 63–77%. This indicates the stability and robustness of the calibration.

In contrast, the vibration problem exhibits significantly higher sensitivity. A $\pm$ 5% variation in L_C increases the objective function by approximately 400–430%, while a $\pm$ 10% perturbation results in an increase exceeding 1500–1800%. This sharp increase demonstrates that the objective function possesses a highly pronounced minimum, indicating that the parameter is strongly constrained by the dynamic response.

The results clearly show that deviations of L_C from its calibrated value lead to a systematic increase in the objective function. For both bending and vibration problems, a $\pm$ 5% perturbation results in an increase of approximately 20–40% relative to the minimum value, while a $\pm$ 10% perturbation leads to a substantially larger increase, exceeding 70–100%. This behavior indicates a pronounced deterioration in the quality of fit when the parameter deviates from its optimal value.

In addition, perturbation tests were performed for the remaining parameters L_l and α. The results show that small variations ($\pm 5\%$) in these parameters also lead to an increase in the objective function, confirming that they are well constrained by the MD data. In particular, the parameter α exhibits high sensitivity despite its small statistical dispersion, indicating strong identifiability. These observations are consistent with the low coefficients of variation reported in Table C.1 and further support the robustness and stability of the calibration procedure.

Data availability

Data will be made available on request.

References

[1] Shao B, Lu C, Xiang Y, Li F, Song M. Comprehensive review of RF MEMS switches in satellite communications. Sensors 2024;24:3135. https://doi.org/10.3390/s24103135.
[2] Kumar A, Varghese A, Kalra D, Raunak A, Prasad Jaiverdhan M, Janyani V, Yadav RP. MEMS-based piezoresistive and capacitive microphones: a review on materials and methods. Mater Sci Semicond Process 2024;169:107879. https://doi.org/10.1016/j.mssp.2023.107879.
[3] Liu J, Liu H. Research on flexible sensors for wearable devices: a review. Nanomaterials 2025;15:520. https://doi.org/10.3390/nano15070520.
[4] Lv J, Zhang C, Liu J, Li W, Wu Z. High-stability and high-sensitivity graphene MEMS force sensor. Measurement 2025;256:118258. https://doi.org/10.1016/j.measurement.2025.118258.
[5] Zhao Y, Li Z, Xia Y, Jia Q, Zhao L, Maboudia R. Advances in micro- and nano-scale resonant mass-sensitive gas sensors: mechanisms, materials, functionalization and applications. Sens Actuators B: Chem 2025;431:137415. https://doi.org/10.1016/j.snb.2025.137415.
[6] Huang W, Zhang Y, Gao X, He Y, Wu X, Zhao R, Yu T. Micro-electro-mechanical system sensors in robotic perception and control. Sens Actuators A: Phys 2026;405:117788. https://doi.org/10.1016/j.sna.2026.117788.
[7] Zhang Z, Zhang H, Hao Y, Chang H. A review on MEMS silicon resonant accelerometers. J Microelectromechanical Syst 2024;33:174–208. https://doi.org/10.1109/JMEMS.2024.3354235.
[8] Mahmood MRashid, Griesmann J, Chervenkov S, Yilmaz M. Alignment teaching assisted fully automated mechanical dicing of MEMS and NEMS devices. J Micromech Microeng 2025;35:055001. https://doi.org/10.1088/1361-6439/adc9bb.

[9] Xiao M, Xu A, Sui Z, Zhang W, Liu H, Lee C. Multifunctional MEMS, NEMS, micro/nano-structures enabled by piezoelectric and ferroelectric effects. Nanoscale Horiz 2025;10:2744–71. https://doi.org/10.1039/D5NH00386E.
[10] Stapf H, Selbmann F, Joseph Y, Rahimi P. Membrane-based NEMS/MEMS biosensors. ACS Appl Electron Mater 2024;6:2120–33. https://doi.org/10.1021/acsaelm.3c01732.
[11] Yücer S, Sarac B, Adıgüzel B, Ciftci F. Wearable electronic patch for physicochemical data transmission: mXene-based MEMS/NEMS biosensors. Mater Today Phys 2026;62:102040. https://doi.org/10.1016/j.mtphys.2026.102040.
[12] Pachkawade V. Transduction in M/NEMS—actuation and sensing: a review. IEEE Sens J 2024;24:7420–31. https://doi.org/10.1109/JSEN.2024.3356562.
[13] Hayashi S, Cameron C, Gutschmidt S, Murray R, Krauskopf B. Experimentally characterising the dynamical landscape of an active MEMS cantilever. Commun Eng 2025;4:211. https://doi.org/10.1038/s44172-025-00537-9.
[14] Fan X, He C, Ding J, Gao Q, Ma H, Lemme MC, Zhang W. Graphene MEMS and NEMS. Microsyst Nanoeng 2024;10:154. https://doi.org/10.1038/s41378-024-00791-5.
[15] Cuenot S, Frétigny C, Demoustier-Champagne S, Nysten B. Surface tension effect on the mechanical properties of nanomaterials measured by atomic force microscopy. Phys Rev B 2004;69:165410. https://doi.org/10.1103/PhysRevB.69.165410.
[16] Babaei Gavan K, Westra HJR, van der Drift EWJM, Venstra WJ, van der Zant HSJ. Size-dependent effective Young's modulus of silicon nitride cantilevers. Appl Phys Lett 2009;94:233108. https://doi.org/10.1063/1.3152772.
[17] A.M. Abazari, S.M. Safavi, G. Rezazadeh, L.G. Villanueva, Size effects on mechanical properties of micro/nano structures, (2015). https://doi.org/10.48550/arXiv.1508.01322.
[18] Kim J-Y, Greer JR. Size-dependent mechanical properties of molybdenum nanopillars. Appl Phys Lett 2008;93:101916. https://doi.org/10.1063/1.2979684.
[19] Darban H. MD benchmarks: size-dependent tension, bending, buckling, and vibration of nanobeams. Int J Mech Sci 2025;296:110316. https://doi.org/10.1016/j.ijmecsci.2025.110316.
[20] Li J, Accardo A, Liu S. Size effect in the compression of 3D polymerized microstructures. J Appl Mech 2024;91. https://doi.org/10.1115/1.4063028.
[21] Yang J, Han P, Yang F, Chi H, Cheng Z, Wang X. Revealing the mechanism of size effect on the forming limit of TA1 pure titanium foil at micro/meso scale through microstructure evolution. J Alloys Compd 2025;1040:183706. https://doi.org/10.1016/j.jallcom.2025.183706.
[22] Hori R, Fujita K, Chen CY, Kurioka T, Wu J-Y, Chang T-FM, Machida K, Ito H, Miyake Y, Sone M. Cross-sectional geometry effect on bending strength of gold micro-cantilever with trapezoidal cross-section. Micro Nano Eng 2024;23:100259. https://doi.org/10.1016/j.mne.2024.100259.
[23] Geng D, Yu H, Ando M, Tanigawa H, Kurotaki H, Nozawa T, Kondo S, Kasada R. Size dependence of micro-scale mechanical properties on heavy-ion irradiated tempered-martensitic steel evaluated through nanoindentation and micropillar compression tests. J Nucl Mater 2024;593:155013. https://doi.org/10.1016/j.jnucmat.2024.155013.
[24] Lee B. First-principles calculation of mechanical properties of Si⟨001⟩ nanowires and comparison to nanomechanical theory. Phys Rev B 2007;75. https://doi.org/10.1103/PhysRevB.75.195328.
[25] Kim Y-J, Son K, Choi I-C, Choi I-S, Park WI, Jang J. Exploring nanomechanical behavior of silicon nanowires: AFM bending versus nanoindentation. Adv Funct Mater 2011;21:279–86. https://doi.org/10.1002/adfm.201001471.
[26] Chen Y, Stevenson I, Pouy R, Wang L, McIlroy DN, Pounds T, Norton MGrant, Aston DEric. Mechanical elasticity of vapour–liquid–solid grown GaN nanowires. Nanotechnology 2007;18:135708. https://doi.org/10.1088/0957-4484/18/13/135708.
[27] Li X, Ono T, Wang Y, Esashi M. Ultrathin single-crystalline-silicon cantilever resonators: fabrication technology and significant specimen size effect on Young's modulus. Appl Phys Lett 2003;83:3081–3. https://doi.org/10.1063/1.1618369.
[28] Nilsson SG, Borrisé X, Montelius L. Size effect on Young's modulus of thin chromium cantilevers. Appl Phys Lett 2004;85:3555–7. https://doi.org/10.1063/1.1807945.
[29] Broughton JQ, Meli CA, Vashishta P, Kalia RK. Direct atomistic simulation of quartz crystal oscillators: bulk properties and nanoscale devices. Phys Rev B 1997;56:611–8. https://doi.org/10.1103/PhysRevB.56.611.
[30] Lam DCC, Yang F, Chong ACM, Wang J, Tong P. Experiments and theory in strain gradient elasticity. J Mech Phys Solids 2003;51:1477–508. https://doi.org/10.1016/S0022-5096(03)00053-X.
[31] Jing GY, Duan HL, Sun XM, Zhang ZS, Xu J, Li YD, Wang JX, Yu DP. Surface effects on elastic properties of silver nanowires: contact atomic-force microscopy. Phys Rev B 2006;73:235409. https://doi.org/10.1103/PhysRevB.73.235409.
[32] Lei J, He Y, Guo S, Li Z, Liu D. Size-dependent vibration of nickel cantilever microbeams: experiment and gradient elasticity. AIP Adv 2016;6:105202. https://doi.org/10.1063/1.4964660.
[33] Chen SH, Feng B. Size effect in micro-scale cantilever beam bending. Acta Mech 2011;219:291–307. https://doi.org/10.1007/s00707-011-0461-7.
[34] McFarland AW, Colton JS. Role of material microstructure in plate stiffness with relevance to microcantilever sensors. J Micromech Microeng 2005;15:1060–7. https://doi.org/10.1088/0960-1317/15/5/024.
[35] Tan EPS, Zhu Y, Yu T, Dai L, Sow CH, Tan VBC, Lim CT. Crystallinity and surface effects on Young's modulus of CuO nanowires. Appl Phys Lett 2007;90:163112. https://doi.org/10.1063/1.2723654.
[36] Arzt E. Size effects in materials due to microstructural and dimensional constraints: a comparative review. Acta Mater 1998;46:5611–26. https://doi.org/10.1016/S1359-6454(98)00231-6.
[37] Zhu TT, Bushby AJ, Dunstan DJ. Materials mechanical size effects: a review. Mater Technol 2008;23:193–209. https://doi.org/10.1179/175355508X376843.
[38] Miller RE, Shenoy VB. Size-dependent elastic properties of nanosized structural elements. Nanotechnology 2000;11:139–47. https://doi.org/10.1088/0957-4484/11/3/301.
[39] Cammarata RC. Surface and interface stress effects in thin films. Prog Surf Sci 1994;46:1–38. https://doi.org/10.1016/0079-6816(94)90005-1.
[40] Roduner E. Size matters: why nanomaterials are different. Chem Soc Rev 2006;35:583. https://doi.org/10.1039/B502142C.
[41] Cammarata RC. Surface and interface stress effects on interfacial and nanostructured materials. Mater Sci Eng: A 1997;237:180–4. https://doi.org/10.1016/S0921-5093(97)00128-7.
[42] CAO G, CHEN X. Size dependence and orientation dependence of elastic properties of ZnO nanofilms. Int J Solids Struct 2008;45:1730–53. https://doi.org/10.1016/j.ijsolstr.2007.10.019.
[43] Zhang C, Chen W, Zhang Ch. Two-dimensional theory of piezoelectric plates considering surface effect. Eur J Mech - A/Solids 2013;41:50–7. https://doi.org/10.1016/j.euromechsol.2013.02.005.
[44] Zhang C, Zhu J, Chen W, Zhang Ch. Two-dimensional theory of piezoelectric shells considering surface effect. Eur J Mech - A/Solids 2014;43:109–17. https://doi.org/10.1016/j.euromechsol.2013.09.007.
[45] Zhou LG, Huang H. Are surfaces elastically softer or stiffer? Appl Phys Lett 2004;84:1940–2. https://doi.org/10.1063/1.1682698.
[46] Miller RE, Shenoy VB. Size-dependent elastic properties of nanosized structural elements. Nanotechnology 2000;11:139–47. https://doi.org/10.1088/0957-4484/11/3/301.
[47] Eringen AC. Nonlocal polar elastic continua. Int J Eng Sci 1972;10:1–16. https://doi.org/10.1016/0020-7225(72)90070-5.
[48] Mindlin RD, Eshel NN. On first strain-gradient theories in linear elasticity. Int J Solids Struct 1968;4:109–24. https://doi.org/10.1016/0020-7683(68)90036-X.
[49] Yang F, Chong ACM, Lam DCC, Tong P. Couple stress based strain gradient theory for elasticity. Int J Solids Struct 2002;39:2731–43. https://doi.org/10.1016/S0020-7683(02)00152-X.
[50] Mindlin RD, Tiersten HF. Effects of couple-stresses in linear elasticity. Arch Ration Mech Anal 1962;11:415–48. https://doi.org/10.1007/BF00253946.
[51] Toupin RA. Elastic materials with couple-stresses. Arch Ration Mech Anal 1962;11:385–414. https://doi.org/10.1007/BF00253945.
[52] Gurtin ME, Murdoch AIan. A continuum theory of elastic material surfaces. Arch Ration Mech Anal 1975;57:291–323. https://doi.org/10.1007/BF00261375.
[53] Gurtin ME, Murdoch AIan. Surface stress in solids. Int J Solids Struct 1978;14:431–40. https://doi.org/10.1016/0020-7683(78)90008-2.
[54] Eringen AC. Linear theory of micropolar elasticity. J Math Mech 1966;15:909–23.
[55] Peddieson J, Buchanan GR, McNitt RP. Application of nonlocal continuum models to nanotechnology. Int J Eng Sci 2003;41:305–12. https://doi.org/10.1016/S0020-7225(02)00210-0.
[56] Romano G, Barretta R. Nonlocal elasticity in nanobeams: the stress-driven integral model. Int J Eng Sci 2017;115:14–27. https://doi.org/10.1016/j.ijengsci.2017.03.002.
[57] Barretta R, Marotti de Sciarra F. Variational nonlocal gradient elasticity for nanobeams. Int J Eng Sci 2019;143:73–91. https://doi.org/10.1016/j.ijengsci.2019.06.016.
[58] Yang W, Wang S, Kang W, Yu T, Li Y. A unified high-order model for size-dependent vibration of nanobeam based on nonlocal strain/stress gradient elasticity with surface effect. Int J Eng Sci 2023;182:103785. https://doi.org/10.1016/j.ijengsci.2022.103785.
[59] Caporale A, Darban H, Luciano R. Nonlocal strain and stress gradient elasticity of Timoshenko nano-beams with loading discontinuities. Int J Eng Sci 2022;173:103620. https://doi.org/10.1016/j.ijengsci.2021.103620.
[60] Penna R, Feo L, Lovisi G. Hygro-thermal bending behavior of porous FG nanobeams via local/nonlocal strain and stress gradient theories of elasticity. Compos Struct 2021;263:113627. https://doi.org/10.1016/j.compstruct.2021.113627.
[61] Darban H, Luciano R, Caporale A, Basista M. Modeling of buckling of nanobeams embedded in elastic medium by local-nonlocal stress-driven gradient elasticity theory. Compos Struct 2022;297:115907. https://doi.org/10.1016/j.compstruct.2022.115907.
[62] Wang S, Ding W, Li Z, Xu B, Zhai C, Kang W, Yang W, Li Y. A size-dependent quasi-3D model for bending and buckling of porous functionally graded curved nanobeam. Int J Eng Sci 2023;193:103962. https://doi.org/10.1016/j.ijengsci.2023.103962.
[63] Sun X, Ilanko S, Mochida Y, Tighe RC. A study on the feasibility of natural frequency-based crack detection. Appl Sci 2024;14:11712. https://doi.org/10.3390/app142411712.
[64] Darban H, Fabbrocino F, Luciano R. Size-dependent linear elastic fracture of nanobeams. Int J Eng Sci 2020;157:103381. https://doi.org/10.1016/j.ijengsci.2020.103381.
[65] Wang H, Li X, Tang G, Shen Z. Effect of surface stress on stress intensity factors of a nanoscale crack via double cantilever beam model. J Nanosci Nanotechnol 2013;13:477–82. https://doi.org/10.1166/jnn.2013.6737.
[66] Zhang H, Li XF, Tang GJ, Shen ZB. Stress intensity factors of double cantilever nanobeams via gradient elasticity theory. Eng Fract Mech 2013;105:58–64. https://doi.org/10.1016/j.engfracmech.2013.03.005.

[67] Hirakata H, Nishijima O, Fukuhara N, Kondo T, Yonezu A, Minoshima K. Size effect on fracture toughness of freestanding copper nano-films. Mater Sci Eng: A 2011;528:8120–7. https://doi.org/10.1016/j.msea.2011.07.071.
[68] Cheng Y, Yu L, Chen L, Liu W, Yi X, Duan H. Failure of fracture toughness criterion at small scales. Phys Rev Mater 2019;3:113602. https://doi.org/10.1103/PhysRevMaterials.3.113602.
[69] Taloni A, Vodret M, Costantini G, Zapperi S. Size effects on the fracture of microscale and nanoscale materials. Nat Rev Mater 2018;3:211–24. https://doi.org/10.1038/s41578-018-0029-4.
[70] Zhang P, Schiavone P, Qing H, Li Q. Stress-driven nonlocal integral model with discontinuities for transverse vibration of multi-cracked non-uniform Timoshenko beams with general boundary conditions. Compos Struct 2025;353:118712. https://doi.org/10.1016/j.compstruct.2024.118712.
[71] Fan T. Vibration of cracked Timoshenko nanobeam with flexoelectric effects. Mech Based Des Struct Mach 2025;54:2515243. https://doi.org/10.1080/15397734.2025.2515243.
[72] Attia MA, Matbuly MS, Osman T, AbdElkhalek M. Dynamic analysis of double cracked bi-directional functionally graded nanobeam using the differential quadrature method. Acta Mech 2024;235:1961–2012. https://doi.org/10.1007/s00707-023-03797-8.
[73] Akbas SD. Bending of a cracked functionally graded nanobeam. Adv Nano Res 2018;6:219–42. https://doi.org/10.12989/anr.2018.6.3.219.
[74] Soltanpour M, Ghadiri M, Yazdi A, Safi M. Free transverse vibration analysis of size dependent Timoshenko FG cracked nanobeams resting on elastic medium. Microsyst Technol 2017;23:1813–30. https://doi.org/10.1007/s00542-016-2983-3.
[75] Loya J, López-Puente J, Zaera R, Fernández-Sáez J. Free transverse vibrations of cracked nanobeams using a nonlocal elasticity model. J Appl Phys 2009;105:044309. https://doi.org/10.1063/1.3068370.
[76] Esen I, Özarpa C, Eltaher MA. Free vibration of a cracked FG microbeam embedded in an elastic matrix and exposed to magnetic field in a thermal environment. Compos Struct 2021;261:113552. https://doi.org/10.1016/j.compstruct.2021.113552.
[77] Dastjerdi S, Abbasi M. A vibration analysis of a cracked micro-cantilever in an atomic force microscope by using transfer matrix method. Ultramicroscopy 2019;196:33–9. https://doi.org/10.1016/j.ultramic.2018.09.014.
[78] Fu M, Shi Z, Bošnjak B, Blick RH, Scheer E, Yang F. Silicon-based MEMS/NEMS empowered by graphene: a scheme for large tunability and functionality. Microsyst Nanoeng 2025;11:116. https://doi.org/10.1038/s41378-025-00960-0.
[79] Zhu J, Liu X, Shi Q, He T, Sun Z, Guo X, Liu W, Sulaiman OB, Dong B, Lee C. Development trends and perspectives of future sensors and MEMS/NEMS. Micromachines 2020;11:7. https://doi.org/10.3390/mi11010007.
[80] Sadeghian H, Yang C-K, Goosen JFL, Bossche A, Staufer U, French PJ, van Keulen F. Effects of size and defects on the elasticity of silicon nanocantilevers. J Micromech Microeng 2010;20:064012. https://doi.org/10.1088/0960-1317/20/6/064012.
[81] Azadbakht J, Nejat Pishkenari H. Properly-tuned continuum and atomistic models for vibrational analysis of the silicon nanoplates. Int J Mech Sci 2022;229:107517. https://doi.org/10.1016/j.ijmecsci.2022.107517.
[82] Darban H, Luciano R, Basista M. Calibration of the length scale parameter for the stress-driven nonlocal elasticity model from quasi-static and dynamic experiments. Mech Adv Mater Struct 2023;30:3518–24. https://doi.org/10.1080/15376494.2022.2077488.
[83] Ballestra A, Brusa E, De Pasquale G, Munteanu MGh, Somà A. FEM modelling and experimental characterization of microbeams in presence of residual stress. Analog Integr Circ Sig Process 2010;63:477–88. https://doi.org/10.1007/s10470-009-9420-9.
[84] Nam C-Y, Jaroenapibal P, Tham D, Luzzi DE, Evoy S, Fischer JE. Diameter-dependent electromechanical properties of GaN nanowires. Nano Lett 2006;6:153–8. https://doi.org/10.1021/nl051860m.
[85] Babaei Gavan K, Westra HJR, van der Drift EWJM, Venstra WJ, van der Zant HSJ. Size-dependent effective Young's modulus of silicon nitride cantilevers. Appl Phys Lett 2009;94:233108. https://doi.org/10.1063/1.3152772.
[86] Liebold C, Müller WH. Comparison of gradient elasticity models for the bending of micromaterials. Comput Mater Sci 2016;116:52–61. https://doi.org/10.1016/j.commatsci.2015.10.031.
[87] Choi J-H, Kim H, Kim J-Y, Lim K-H, Lee B-C, Sim G-D. Micro-cantilever bending tests for understanding size effect in gradient elasticity. Mater Des 2022;214:110398. https://doi.org/10.1016/j.matdes.2022.110398.
[88] Yokoyama T, Chen M-C. Vibration analysis of edge-cracked beams using a line-spring model. Eng Fract Mech 1998;59:403–9. https://doi.org/10.1016/S0013-7944(97)80283-4.
[89] Hassanpour A, Darban H. Softening and stiffening size effects in free flexural vibration of small-scale cracked beams. J Sound Vib 2025;612:119135. https://doi.org/10.1016/j.jsv.2025.119135.
[90] Plimpton S. Fast parallel algorithms for short-range molecular dynamics. J Comput Phys 1995;117:1–19. https://doi.org/10.1006/jcph.1995.1039.
[91] Stillinger FH, Weber TA. Computer simulation of local order in condensed phases of silicon. Phys Rev B 1985;31:5262–71. https://doi.org/10.1103/PhysRevB.31.5262.
[92] Zhu T, Li J, Yip S. Atomistic characterization of three-dimensional lattice trapping barriers to brittle fracture. Proc A 2006;462:1741–61. https://doi.org/10.1098/rspa.2005.1567.
[93] Balamane H, Halicioglu T, Tiller WA. Comparative study of silicon empirical interatomic potentials. Phys Rev B 1992;46:2250–79. https://doi.org/10.1103/PhysRevB.46.2250.
[94] Spence JCH, Huang YM, Sankey O. Lattice trapping and surface reconstruction for silicon cleavage on (111). *Ab-initio* quantum molecular dynamics calculations. Acta Metall Mater 1993;41:2815–24. https://doi.org/10.1016/0956-7151(93)90096-B.
[95] Huang S, Zhang S, Belytschko T, Terdalkar SS, Zhu T. Mechanics of nanocrack: fracture, dislocation emission, and amorphization. J Mech Phys Solids 2009;57:840–50. https://doi.org/10.1016/j.jmps.2009.01.006.
[96] Pishkenari HN, Afsharmanesh B, Akbari E. Surface elasticity and size effect on the vibrational behavior of silicon nanoresonators. Curr Appl Phys 2015;15:1389–96. https://doi.org/10.1016/j.cap.2015.08.002.
[97] Vogl LM, Schweizer P, Richter G, Spiecker E. Effect of size and shape on the elastic modulus of metal nanowires. MRS Adv 2021;6:665–73. https://doi.org/10.1557/s43580-021-00103-3.
[98] Patel BN, Srinivasan SM. Novel nickle foil micro-bend tests and the need for a relook at length scale parameter's numerical value. Mech Adv Mater Struct 2022;29:3924–33. https://doi.org/10.1080/15376494.2021.1913771.
[99] McDowell MT, Leach AM, Gall K. Bending and tensile deformation of metallic nanowires. Model Simul Mater Sci Eng 2008;16:045003. https://doi.org/10.1088/0965-0393/16/4/045003.
[100] Xu F, Qin Q, Mishra A, Gu Y, Zhu Y. Mechanical properties of ZnO nanowires under different loading modes. Nano Res 2010;3:271–80. https://doi.org/10.1007/s12274-010-1030-4.
[101] Singh A, Singh G. A localized stress field approach for calculating the critical stress intensity factor for an isotropic solid at atomistic scale. Mech Mater 2023;181:104632. https://doi.org/10.1016/j.mechmat.2023.104632.
[102] Caporale A, Darban H, Luciano R. Nonlocal strain and stress gradient elasticity of Timoshenko nano-beams with loading discontinuities. Int J Eng Sci 2022;173:103620. https://doi.org/10.1016/j.ijengsci.2021.103620.